# Simultaneous EEG and fMRI recording in small animals

by

**Akira Sumiyoshi**

A thesis submitted for the degree of Doctor of Philosophy

at Tohoku University School of Medicine

March 2011

# ABSTRACT

**"Simultaneous EEG and fMRI recording in small animals"**

submitted by

**Akira Sumiyoshi**

Advisors: Jorge J. Riera and Ryuta Kawashima

Simultaneous recording of electroencephalography (EEG) and functional magnetic resonance imaging (fMRI) is now widely accepted as a prevailing tool to study brain functions. For over a decade, EEG caps with high-density arrays of electrodes for EEG–fMRI studies in humans have been academically and even commercially available. However, simultaneous EEG and fMRI recording in small animals has been limited to only a few electrodes for mainly two technical reasons; i.e. the small available scalp area and the proximity of the electrodes to the brain tissue. In addition, the MRI template set, necessary for spatial normalization in fMRI analyses, is incomplete in terms of applicability compared to template sets for humans, which makes it critically difficult to perform statistical fMRI analyses in small animals. Animals subjects offer distinct experimental advantages compared to human subjects, e.g. invasive physiological monitoring, pharmacological intervention, wide genetic variants; therefore, it is important to establish an experimental protocol for animal models, especially in rodents, i.e. rats and mice.

Here I firstly introduce a new EEG mini-cap and a protocol for obtaining whole scalp EEG recordings simultaneously with 7 T fMRI signals in small animals. I provide methodological protocol for evaluating a number of problems emerging from the particulars of using rodents in simultaneous EEG and fMRI recording. The quality and reproducibility of both EEG and fMRI signals were demonstrated using a conventional forepaw stimulation paradigm in Wistar rats. Based on this quantitative analysis, I conclude that simultaneous EEG–fMRI recordings are achievable in small animals without significant EEG/fMRI signal loss. Secondly, I present a new MRI Wistar rat template set in the latest version of the Paxinos & Watson (P&W) atlas space comprising: 1) an average of 30 T2-weighted MRIs, 2) an image with 96 digitalized cortical structures of the P&W atlas, with several advantages over those reported in the literature, e.g. ROI-based connectivity analysis. The new template set's usefulness is exemplified by the correct spatial location of forepaw and hindpaw fMRI activations analyzed with digitalized cortical structure interpretations.

Through experimental manipulations, i.e. invasive physiological monitoring and advanced drug administration protocols, the proposed methodologies have become remarkably valuable in studying the fundamental mechanisms of healthy brains as well as those associated with diseases. Not only in basic neuroscience, but these methodologies may be remarkable as a future experimental platform for preclinical drug screening in the pharmaceutical industry.

# CONTENTS

# SECTION 1 INTRODUCTION

## 1.1 Overview of multimodal data integration

In the second half of the twentieth century, especially since the 1990's, rapid development of non-invasive functional brain imaging modality has been achieved[1) 2) 3)]. For instance, fMRI, EEG, MEG, and PET/SPECT are currently the most prevalent non-invasive techniques that allow experimental and clinical neuroscientists to achieve their objectives starting from *in vivo* measurements of human brain activity. In line with these technical advances, neuroscientists seem to freely choose one modality from this pool to verify their own hypotheses, taking into account benefits from dissimilarities in the temporal and spatial resolution of each modality (Figure. 1.1).

However, in a system as complex as the brain, one cannot gain a full view of events if one utilizes a single observation technique. Therefore, achievement of the ultimate goal of completely understanding brain activity will require the integration of a variety of observation modalities. Multimodal imaging measurements, whereby data is gathered from various types of instruments, has arisen from this realization; even if some events are best described in one modality, the investigator may also be interested in another modality. Table 1.1 gives an overview of currently available simultaneous multimodal methods and the original reference of the first attempt at each method.

The integration of different measurement modalities can be achieved in a variety of ways, reflecting both the level of synchrony between the data acquired for each modality and the ways in which the data from each modality are used to analyze or interpret findings. The following section summarizes the advantages of multimodal data integration from the literature. Data integration can be divided into three classifications.

**1) Spatial cross-validation**: Cross-validation of measurements (e.g. EEG/MEG dipole source analysis vs. fMRI/PET/SPECT) is one of the motivations for multimodal imaging. In this case, the distribution of brain activity obtained independently from a number of different modalities is compared[4) 5)].

**2) Mutual constraint**: A more advanced form of multimodal data integration than spatial validation is the use of data from one modality in the analysis of data from another modality. This can be either spatially- or temporally-based[6) 7)]. In the spatial domain, activated brain regions identified using fMRI or PET data have been used as constraints, or priors, for the solution to the EEG/MEG inverse problem[8) 9) 10)]. In the temporal domain, EEG usually provides the onset(s) of the imaging study of spontaneous activity (especially that obtained in simultaneous EEG and fMRI acquisitions). This can be seen in literature about the study of epilepsy[11) 12)] , brain rhythms[13) 14) 15)], and sleep[16)].

**3) Model-based data fusion**: Some investigators have proposed a more fundamental approach to data integration aimed at creating a biophysical model that relates data from each

modality within a unified framework in order to overcome current limitations in the interpretation of multimodal data and ultimately relate observations to fundamental brain mechanisms[17) 18) 19) 20) 21) 22)].

As any single imaging method is limited to observing a limited aspect of brain function, multimodal brain imaging is a key tool for gaining a comprehensive understanding of brain activity. Therefore, the combination of information about the electrical activity of the brain with data of the spatially superior corresponding hemodynamic changes represents one of the most powerful examples of multimodal imaging techniques. It is surely capable of providing new insights into brain function[23) 24)].

### 1.2 Physiological basis of functional imaging modality

#### 1.2.1 EEG: origin and measurement

EEG is the recording of summed electrical activity along the scalp produced by the firing of a population of neurons within the brain[25)]. In general, neuronal activation can be distinguished by two main forms[26)]: the fast depolarization of the neuronal membranes, which results in an action potential mediated by sodium and potassium voltage-dependent ionic conductance, and the slower changes in membrane potential due to synaptic activation, as mediated by several neurotransmitter systems. The action potential consists of a rapid change in membrane potential such that the intracellular potential suddenly jumps from negative to positive, and quickly (in 1 or 2 ms) returns to the resting intracellular negativity. In this way,

an impulse is generated that has the remarkable property of propagating along axons and dendrites without any loss of amplitude. Regarding the slower postsynaptic potentials, two main kinds must be distinguished: the excitatory (EPSPs) and the inhibitory (IPSPs) potentials. These potentials depend on the neurotransmitter and corresponding receptor type and on their interactions with specific ionic channels and/or intracellular second messengers. In the case of EPSP, the transmembrane current is carried by positive ions inwards (e.g. $Na^+$, $Ca^{2+}$), whereas the current is carried by negative ions inwards (e.g. $Cl^-$) or positive ions outwards in the case of IPSP. Thus, an active sink is generated in the extracellular medium at the level of the excitatory synapse, whereas an active source occurs in the case of the inhibitory synapse. However, the electric potentials generated by single neurons are far too small and desynchronized to be recorded by EEG or MEG. EEG activity, therefore, always reflects the summation of the synchronous activity of thousands or millions of neurons that have similar spatial orientations. If the cells do not have similar spatial orientations, their ions do not line up and create detectable net currents. Pyramidal neurons of the cortex are thought to produce most EEG signals because they are arranged in palisades with the apical dendrites aligned perpendicularly to the cortical surface. It may not be surprising that the mechanism of EEG generation remained controversial for a relatively long time considering the complexity of the underlying systems of neuronal generators and the rather involved transfer of signals from the cortical surface to the scalp due to the topological and electrical properties of the local tissue

on the micro-scale (e.g. orientations of myelinated axons)[27] and the macro-scale (brain, cerebrospinal fluid, skull, and scalp)[28) 29)].

### 1.2.2 fMRI

#### 1.2.2.1 The basics of MR imaging

In MRI, the signal that is measured usually arises from the nuclei of the hydrogen atoms (i.e. protons), which posses a physical property, its spin. Each spin has a small magnetic dipole moment and they align in an external magnetic field. If tissue is brought into the MR scanner, proton spins (mainly from water) will align either anti-parallel or parallel to the magnetic field. A tiny majority of the spins assume the latter alignment (i.e. parallel to the static field) and their magnetic moments add up, giving rise to a net macroscopic magnetization, representing a state of equilibrium. If the protons inside the magnetic field are exposed to an electromagnetic wave (i.e. RF) with a specific frequency, the Larmor frequency, the magnetization will tilt in proportion to the exposure duration. The tilted magnetization then rotates around the magnetic field vector (i.e. precession). During precession, the protons send out an electromagnetic wave that has the Larmor frequency, which is proportional to the magnetic field, with a value of 42.6 MHz/T. It should be noted that the tilted magnetization gradually returns to its original state after the electromagnetic wave stimulation ceases (i.e. *relaxation*). The tilting of the magnetization only works if the frequency of the transmitted

electromagnetic signal exactly equals the proton Larmor frequency, which denotes the foundation of the NMR phenomenon[30) 31)].

**Relaxation times T1 and T2**: After an RF pulse has tilted the magnetization vector, precession takes place. However, precession has a limited duration: after a while, the magnetization is supposed to, once again, be parallel to the static magnetic field, i.e. at stable equilibrium. This process is called *relaxation*. Relaxation consists of two simultaneous processes as follow. The longitudinal component of the tilted magnetization (i.e. the component parallel to the magnetic field) approaches a maximum value (the so-called equilibrium value) with the time constant T1, *the longitudinal relaxation time*. This process is also called *spin-lattice relaxation* because free water spins transfer energy to the surrounding environment, the lattice. The transverse component of the tilted magnetization (i.e. the component perpendicular to the magnetic field) vanishes with the time constant T2, *the transverse relaxation tim*e. This process is also called *spin-spin relaxation* because free water spins exchange small amounts of energy.

**Relaxation time T2***: The occurrence of GE is a striking phenomenon in MR techniques and GE methods are widely used, in particular for functional imaging. Directly after the RF pulse, the magnetization vectors of the excited spins all point in the same direction. Together they total a strong net magnetization that gives rise to a strong signal. While the gradient is switched on in the *x*-direction, spins at different positions in space will be exposed to different

field strengths so they rotate with different Larmor frequencies (*the spin dephase*). Hence, their contributions to the net magnetization cancel each other causing fast signal decay. In general, it can be said that any inhomogeneity of the static magnetic field will have a similar effect that results in accelerated signal decay. The signal decays with the *effective (apparent) transverse relaxation time T2** thus depend on the degree of field inhomogeneity and can be considerably shorter than T2. After gradient inversion, the distribution of field strengths will be reversed. A spin ensemble that initially rotated quickly will now continue with a low frequency, and a spin ensemble that initially rotated slowly will continue with a high frequency. This process continually reduces the phase difference between spins, so that the spins are rephased and the resulting signal accumulates, attaining maximum strength when the vectors are in their initial phase again. The time difference between the initial RF pulse and the center of the gradient echo is called the echo time TE. It should be noted that the choice of TE determines the T2* contrast: if TE is too short, the spins do not have sufficient time to dephase and the T2* weight will be poor. If TE is considerably longer than T2*, the signal will have decayed by the time the acquisition starts and the SNR of the image will be poor.

#### 1.2.2.2 The BOLD effect and fMRI

Gradient echo techniques are of major importance for functional imaging studies because neuronal activations lead to small changes of T2* in the surrounding brain tissue and thus identify variations in T2*-weighted gradient echo images. This effect is called the BOLD,

which was firstly reported by Ogawa et al., (1990)[32]. Most fMRI imaging studies exploit the intrinsic BOLD contrast mechanism[33) 34) 35)]. In general, it has been observed that signal amplitudes are temporarily enhanced in regions of neuronal activation for brain images based on GE techniques with a suitable echo time, TE. This effect can be explained roughly as follows. The MR signal of brain tissue depends on the level of oxygenation since hemoglobin is diamagnetic when oxygenated (oxyhemoglobin) but paramagnetic when deoxygenated (deoxyhemoglobin). Therefore, higher BOLD signal intensities seem to arise from increases in the concentration of oxygenated hemoglobin[36)]. However, in reality, matters are much more complicated[37)] and the physiology behind these effects is only partially understood[38)]. The multi-cellular component of the brain (i.e. neurons, glia, and vasculature cells) seems to form a metabolic network to sustain brain activity[39) 40) 41) 42) 43)]; however, it is not clear how the coupling between neuronal activity and blood flow (i.e. neuron-to-vascular coupling) is mediated. Studies combining electrophysiology/EEG with fMRI may greatly facilitate the elucidation of such underlying physiological mechanisms[44) 45) 46) 47)].

### 1.3 Simultaneous EEG and fMRI recording

Simultaneous recording of brain activity by different neuroimaging modalities (e.g. EEG and fMRI) can provide additive insights that reach beyond those obtained by each technique individually. This subdivision summarizes the key issues in the recording of EEG and fMRI data in human and animal models, focusing on the historical perspective and the recent technical advances in the field.

#### 1.3.1 EEG–fMRI recording in human subjects

The development of EEG recording during fMRI was motivated by a clinical interest in mapping changes in the neural activity associated with the epileptic discharges observed on surface EEGs onto images of brain anatomy[48]. The initial pace of this technology was slow because conventional EEG equipment is made from metals with magnetic properties that posed concerns about safety[49], the heating of the electrodes during MR scanning[50], and the introduction of artifacts in to the MR images[51]. The initial recordings were done using Grass gold electrodes with long leads connected directly to battery operated EEG preamplifiers[48]. Ives et al., (1993)[48] reported that replacing a conductive cable with a fiber-optic cable eliminates the electromagnetic influence EEG and fMRI have on each other. Subsequent reports established both MRI compatible EEG acquisition hardware and artifact reduction algorithms[49) 52) 53)]. These technical advances have accelerated the rapid development of both academic and commercial EEG–fMRI recording over the last two decades and thus constitute

milestones in EEG–fMRI recording[54) 55) 56) 57)]. To date, several groups have been using simultaneous EEG and fMRI recordings in humans to characterize evoked brain responses [e.g., somatosensory: Christmann et al., (2002)[58)]; auditory: Liebenthal et al., (2003)[59)], visual: Comi et al., (2005)[60)]], resting state [brain rhythms: Goldman et al., (2002)[13)]; sleep: Lövblad et al., (1999)[61)]], and pathological brains [epilepsy: Lemieux et al., (2001)[62)]]. The feasibility of using highly-dense arrays of EEG electrodes on the human scalp inside an MRI scanner has been already demonstrated with up to 128 channels[63)] and the limit of magnetic field strength in EEG–fMRI studies has already reached 7 T[64)]. It should be noted that behind these achievements is the fact that, mainly, Brain Products GmbH (Germany) has made EEG caps with MRI principle-compatible electrodes commercially available. Up to now, more than 170 papers related to EEG–fMRI recordings in humans have been published.

### 1.3.2 EEG–fMRI recording in animal models

The first EEG recording performed during MR scanning in experimental animals was carried out in a cortical spreading depression model in 1995[65)]. It was subsequently followed by a functional activation study in α-chloralose anesthetized Wistar rats using an electrical forepaw/hindpaw stimulation paradigm in 1999. Brinker et al., (1999)[66)] were the first to demonstrate the feasibility of simultaneous measurements of somatosensory evoked cortical potentials and T2*-weighted images in rats. These authors utilized two L-shaped calomel electrodes with their tips introduced into a small nylon nut which was glued to the skull. The

active electrode was inserted at the level of the somatosensory cortex. The authors have insisted that with their setup electrophysiological recording inside the magnet is possible with minimal artifacts. Thereafter, they revealed that T2*-weighted imaging signal intensity increases linearly with somatosensory evoked potential amplitudes. Table 1.4 summarizes EEG–fMRI recording in animal models. Despite the rapid and prevailing advancements in "human" EEG–fMRI recording, the extension of such existing technology to comparative studies in animal models is very limited[67]. This is particularly true for rodents, which are the most beneficial animal models for experimental manipulations. In rodents, only studies with up to a few electrodes made of either calomel or carbon have been possible.

The extention of human EEG–fMRI technology to rodents faces two main obstacles. First, their heads are too small to allocate many classical MRI-compatible electrodes. The traditional method of EEG recording in humans uses silver-based ring-type electrodes fabricated with large areas for the electrolytic-metal interface, i.e. 20–80 $mm^2$ to achieve impedances of less than 5 kΩ[58) 17) 68) 69)]. However, it is impossible to place a dozen of such electrodes on a rodent's head. In one recent work, EEG data was recorded from an array of 32 electrodes allocated on to the heads of mice by means of a perforated Plexiglas grid[70)]. To avoid dry contact between the electrodes and the observation skull area, which would hence reduce electrode impedance to less than 50 kΩ, these authors used 500 μm tips of stainless steel wires immersed in EEG paste. The allocation and fixation of such a dense array of

electrodes on to the head of a rodent lying inside the MRI scanner has never been attempted. The relative distance between the electrodes and the brain tissues constitutes the second obstacle. Assembling large number of electrodes within a few centimeters produces high magnetic field disturbances that will definitely affect any MRI signaling from a brain less than 1 mm away. It has been proven that EEG recording caps in humans disturb magnetic field homogeneity, hence distorting MRI-based images[71) 51) 72)]. Widely used EEG electrodes such as Ag/AgCl, gold-plated silver, platinum, stainless steel, and tin still contain metals that are highly magnetizable by magnetic fields[73)]. Therefore, calibration studies are mandatory whenever new protocols for observing MRI signals in the presence of such metals are introduced. Mullinger et al., (2008)[74)], for example, quantitatively evaluated the characteristics of the static magnetic field ($B_0$-map), excited magnetic field ($B_1$-map), and fMRI time-series for commercially available 32 and 64 electrode caps (EasyCap, Herrsching, Germany) at 1.5, 3, and 7 T in human subjects. In previous studies using rodents, evaluation of the degradation of MRI signals caused by calomel/carbon electrodes was not performed.

Additionally, simultaneous EEG–fMRI studies in experimental animals have to deal with unique problems including issues related to anesthesia and maintaining the physiological stability of the animals for the entire duration of MRI scanning[67)]. Anesthesia must be carefully considered[75)]; many anesthetic agents can alter cerebral hemodynamic response and may alter the neurophysiological behavior under investigation[76) 77)]. Animal movement in the

scanner must be restricted by either chemical muscular blockade[78] or through habituation to a restraining device[79]. Lastly, animal physiology (e.g. $pO_2$, $pCO_2$, and pH) must be carefully monitored during the experiments as the BOLD signal is highly sensitive to the physiological state of the animals[80) 81) 82)]. These obstacles are not relevant to the simultaneous EEG–fMRI studies of awake human subjects and they therefore constitute technological challenges and limitations to extending dozens of human technologies to animal models, especially to those for rats and mice.

**1.4 Advantage of using animal models**

However, animal models offer a number of distinct advantages to human subjects. Specifically, animal models offer:

1) The invasive monitoring of physiological parameters[83].

2) Greater control over the timing and conditions of sensory events[84) 85)].

3) The use of higher magnetic field strength (up to 21.1 T)[86) 87)].

4) The hetero-nuclear magnetic resonance approach (i.e. $^{13}C$, $^{15}N$, $^{17}O$, $^{31}P$)[88) 89) 90)].

5) The use of muscle relaxant for near elimination of movement artifacts[91].

6) A histological validation after *in vivo* experiments[92) 93)].

7) Pharmacological interventions such as phMRI[94].

8) Wide genetic variants (e.g. knock-out/in animals).

9) Less inter-subject variability.

Animal models offer the opportunity to fully utilize the power of EEG–fMRI methods for the noninvasive study of normal and abnormal brain activity. For instance, ictal (seizure) activity can be investigated using animal models[95] and these studies do not have to be limited by movement as the animals can be studied under anaesthetized, paralyzed, and ventilated conditions. Variables affecting brain activity can be better controlled in animals, such as the onset and the type of seizures, the parameters of the ventilator, and the induction and type of anesthesia. Furthermore, invasive studies of electrophysiological, hemodynamical, and histological properties can be performed in animal models to relate fMRI signals to underlying neuronal activity. Thus, simultaneous EEG–fMRI studies of animal models can make an important and/or significant contribution to plenty of neuroscientific questions. Additionally, studies of animal models can provide insight into fMRI signal interpretation[96] (i.e. neuron-to-vascular coupling) and this understanding can be extended to other neuroimaging modalities (e.g. PET, and NIRS).

.

# SECTION 2 MOTIVATION OF THESIS

Current understanding suggests that neuronal and/or astroglial signals transduce changes in neuronal activity into an integrated vascular response which results in a regional increase of blood flow within the activated area (i.e. functional hyperemia). This is the elementary principle for neuroimaging modalities such as fMRI, PET, and NIRS. However, the physiological mechanism of neurovascular coupling is still controversial and unclear[37]. Particularly, the time dependency and relative contribution of each phasic/tonic pathway have not been described yet in the literature[97]. To elucidate these questions, an appropriate animal model is needed to perform pharmacological/physiological interventions during the electrophysiological (i.e. an indicator of neuronal activity such as EEG) and fMRI (an indicator of hemodynamic responses) recordings. The methodology should ultimately use concurrent observations, since both neuronal and fMRI signals are highly sensitive to the physiological states of the animals. In this thesis, I firstly propose a new EEG mini-cap which allows the simultaneous observation of EEG and fMRI signals in small animals. Additionally, I propose a Wistar rat MRI template set which allows the performance of spatial normalization and subsequent statistical fMRI analysis. Combining these methodologies with pharmacological interventions and/or genetic variants in small animals, one can answer the fundamental questions of neuro-to-vascular coupling and those related to pathological conditions.

# SECTION 3 MATERIALS AND METHODS

## 3.1 Animal preparation

All procedures and protocols were performed in agreement with the policies established by the "*Animal Care Committee*" at Tohoku University, Sendai, Japan. The animals were purchased from Charles River, Yokohama, Japan.

### 3.1.1 For the EEG–fMRI experiment

EEG−fMRI experiments were performed in 28 Wistar rats (6 week-old, 211 ± 15 g; $n$ = 5 for the evaluation of both EEG and fMRI signals, $n$ = 6 for the evaluation of T2* mapping, $n$ = 12 for the evaluation of transmitter attenuation, and $n$ = 5 for temperature monitoring). Each rat was anaesthetized with isoflurane (Escain, Mylan, Tokyo, Japan) at 1 l/min oxygenation (5% for initial induction and 3% during surgery). Scalp hair was carefully removed with an electric shaver and a razor. The exposed skin was degreased with 70% ethanol (14712-63, Nacalai Tesque, Kyoto, Japan). The tail vein was catheterized using a 24 G plastic cannula (SR-FF2419, TERUMO, Tokyo, Japan) for systemic and continuous drug delivery through a syringe pump (TOP-5300, TOP, Tokyo, Japan). Each rat was then orally intubated with a 16 G plastic cannula (SR-FF1664, TERUMO, Tokyo, Japan) and mechanically ventilated at around 50 breaths/min under the administration of a muscular relaxation agent[98] (pancuronium bromide, 2 mg/kg/h i.v.; P1918-50MG, Sigma-Aldrich,

Saint Louis, USA). After surgery, each rat was placed in the prone position on a custom built MRI-bed (Bruker Biospin, Ettlingen, Germany) with a bite bar and the anesthesia was switched from isoflurane to α-chloralose[99] (20 mg/kg/h, i.v.; C8849-108, Sigma-Aldrich, Saint Louis, USA). Core body temperature was maintained at 37.0 ± 1 °C during the whole experiment by means of a water-circulating pad (LCH-1K, AS ONE, Osaka, Japan). A pair of small needle electrodes (NE-224S, Nihon Kohden, Tokyo, Japan) were inserted under the skin of the forepaw/hindpaw for electrical stimulation.

**3.1.2 For MRI template construction**

Thirty Wistar rats were used for the MRI template construction. They were distributed in to five groups of six rats for each week of age (6, 7, 8, 9, 10 week-old, body weight ranges of 214 ± 19 g, 275 ± 21 g, 312 ± 9 g, 331 ± 17 g, 364 ± 18 g, respectively). Each rat was initially anesthetized with 5% isoflurane and then secured on a custom-built holder (Bruker Biospin, Ettlingen, Germany) using adhesive tape and a bite bar. A breathing sensor (SA Instruments Inc., NY, USA) was placed under the ventral surface of the rat body. Anesthesia was further maintained with isoflurane (at 1 l/min oxygenation), administered via a face mask. A constant breathing rate was maintained at around 50 breaths/min for the entire span of MRI acquisition by manually maintaining the concentration of isoflurane in the range of 1.5% to 2.5%. This empirical rate is suitable for an MRI acquisition with satisfactorily low motion artifacts and little compromise of the scanning time. Core body temperature was maintained at

37.0 ± 1 °C by means of a hot water-circulating pad.

### 3.2 Physiological monitoring

#### 3.2.1 Temperature monitoring

All temperature measurements were performed using a MRI-compatible temperature probe (Model 1025, SA Instruments, NY, USA). The sensor was inserted in to the rectum and rectal temperature was observed in each MRI experiment.

When RF pulses are applied in MRI experiments, energy is transferred to the proton-spin system. Unfortunately, RF pulses also induce electrical currents in the tissue, which are assumed to be the main source of the unwanted tissue heating. The SAR is the RF power absorbed by the tissue, measured in watts per kilogram of body weight. For the evaluation of head temperature increase caused by the EEG mini-cap, a probe was inserted in the rat's right ear. The location of the probe was confirmed by T1-weighted pilot imaging (Figure 3.1). A temperature experiment was performed if temperature fluctuations were less than ± 0.1 °C for at least 30 min. Temperature monitoring (each 30 s with a resolution of 0.1 °C) was repeated under two different conditions: 1) without the EEG mini-cap and 2) with the connected EEG mini-cap.

#### 3.2.2 Blood pressure/gas monitoring

The left femoral artery was approached from the left inguinal portion. The artery was

clearly dissociated from the nerve and the vein. The distal portion of the artery was tied by a 4-0 silk string and the proximal portion was clamped by forceps. A tiny hole was made on the arterial wall with micro-scissors and a polyethylene catheter (inner diameter: 0.5 mm, outer diameter: 0.8 mm) filled with 100 U/ml heparinized saline solution was then inserted into the hole. The arterial wall and the catheter were fixed by using 4-0 silk string and liquid glue (Vetbond$^{TM}$, 3M, St. Paul, USA). The clamp was released and the lumen of the catheter was flushed with 100 U/ml heparinized saline solution. The process was confirmed by observing the backflow of arterial blood inside the catheter. Arterial blood pressure was digitized by DTXPlus$^{TM}$ (BD, Franklin Lakes, USA) which was connected with the polyethylene catheter, amplified by MEG-6108 (Nihon Kohden, Tokyo, Japan), and analyzed by PowerLab/16SP and LabChart 6 (ADInstruments, Colorado Springs, USA).

Meanwhile, the blood gas sampling was performed as follows: 1) the heparinized saline inside the lumen of the left femoral catheter was removed, 2) 0.3 ml of blood from the catheter was extracted using a 1 ml heparin-coating syringe, 3) the removed saline was returned to the catheter and the lumen of the catheter was flushed with 100 U/ml heparinized saline. The extracted blood was analyzed by Rapidlab248 (Siemens, Munich, Germany) to obtain values of arterial pH, $pO_2$, and $pCO_2$.

### 3.2.3 End-tidal $CO_2$ monitoring

All monitoring of end-tidal $CO_2$ was performed simultaneously under mechanical

ventilation using a commercially available capnograph ($CO_2$ Unit AG-400R, Nihon Koden, Tokyo, Japan). The end-tidal $CO_2$ level was observed and recorded in each fMRI experiment.

### 3.2.4 Ventilator calibration

The tracheotomy during rat fMRI experiments is now widely accepted as a common tool to minimize motion artifacts in the MRI scanner. In fact, many laboratories are employing a combination of the tracheotomy and the administration of muscle relaxation agents[91) 100) 78) 101) 102) 103)]. This is not only for fMRI data quality, it is also beneficial in EEG data quality because any movement of the subject inside the MRI scanner results in an EEG artifact due to the electromagnetic force. However, the circumstances of ventilation (i.e. the ventilator machine itself, the length of the air loop, the pressure of pumping, the respiration rate and so on) are different among many laboratories and therefore calibration of the system needs to be performed before the fMRI experiments. From this standpoint, the variables in the ventilator (SAR-830/AP, CWE Inc., Ardmore, PA, USA) were observed using a water phantom and a parameter table was created (Table 3.1). The physiological variables of all experiments were maintained in the normal limits by making small adjustments to the ventilator (tidal volume = 2.0–2.4 ml, tidal pressure = 10–14 cm $H_2O$).

## 3.3 MRI compatible EEG mini-cap

### 3.3.1 The creation of the EEG mini-cap

For simultaneous EEG and fMRI data acquisition, an EEG mini-cap compatible with MRI and specially designed for rodents was prepared (Figure 3.2). Each electrode in the mini-cap consisted of a movable system with two cylindrical embedded plastic tubes: an inner tube (polyethylene tubing, Fr No. 4, Hibiki, Tokyo, Japan; diameter: 1.33 mm, length: 10 mm) and an external sliding tube (PEEK, 1-8530-04, As One, Osaka, Japan; inner diameter: 1.4 mm, outer diameter: 1.6 mm, length: 6 mm). The inner tube contained liquid-based conductive EEG paste and a platinum wire (purity: 99.98%, PT-351325, Nilaco, Tokyo, Japan; diameter: 0.3 mm, length: 0.8 mm, surface area: 7.67 $mm^2$). The platinum wires were soldered to copper leads. The sliding tubes were spatially-arrayed in a plastic basement (HB-100S-B1, TAIYO ELECTRIC, Hiroshima, Japan) to cover the whole rodent's head with an inter-electrode distance of 3 mm. By means of this system, the inner tube was able to move perpendicularly to the head, which resulted in electrode impedances of less than 50 kΩ. A total of 31 EEG electrodes were utilized in this study and the position of each electrode was individually obtained from the T1-weigthed anatomical reference. All copper leads were connected to a connector box containing current-limiting resistors (Brain Products, Munich, Germany). To avoid EEG contamination from the external electromagnetic field, the lengths of the leads were minimized and the lead wires were twisted together as much as possible along the entire path from the electrode to the amplifier inputs.

### 3.3.2 Properties of EEG gel and paste

Abralyte 2000 conductive gel (EasyCap, Herrsching, Germany) was utilized to attach the electrodes to the scalp. The artifacts caused by the conductive gel were found to be significant[51], hence the minimum amount of gel was used. The EEG paste in the plastic tube was made up of commercially available EEG electrode gel (Biotach, YGB103, GE Healthcare Japan, Tokyo, Japan) (Table 3.2) well-mixed with saline solution (0.9% NaCl) in a volume proportion of 2:1. Note that the EEG paste needs to be carefully adjusted to satisfy conductivity (0.1–1.0 S/m) and viscosity (2–10 Pa•s). For the EEG paste used in the present study, the actual conductivity value was 0.81 S/m at 25 $^{o}$C (B-173, HORIBA, Kyoto, Japan). EEG electrode gel must be carefully selected to warrant appropriate values for magnetic susceptibility and chemical shift, two important parameters for MRI experiments.

### 3.3.3 The phantom preparation

The phantom was constructed from plastic syringes (diameter: 20 mm, length: 60 mm) which contained 21.8 mM $NiCl_2$, 0.5% NaCl and 2.5m% $NaN_3$[104]. This chemical composition was designed to provide T1 and T2 signals comparable to those observed in the gray matter of humans[105]. In order to mimic RF related heating inside the brain, a small amount of NaCl was added to this solution, which increased the conductivity[106]. In the region of contact with the mini-cap, the syringe was covered with standard EEG paste (Abralyte 2000, same as the rat experiment). MRI signals were obtained from this phantom in the presence and absence of the EEG mini-cap. The effects of the EEG mini-cap were evaluated separately in both the RF

transmitter and the receiver circumstances.

### 3.4 Electrophysiology: EEG and ECG

A 32-channel MR-compatible BrainAmp system (Brain Products, Munich, Germany) was used for electrophysiological recordings. EEG signals (31 channels) were amplified, filtered (0.5 Hz high-pass, and 250 Hz low-pass), digitized (5 kHz sampling rate, 0.5 μV resolution) and stored on a hard drive (Software: BrainRecord 1.4, Brain Products, Munich, Germany). An additional channel was used to record the ECG through a needle (Model 1025, SA Instruments, Stony Brook, NY, USA) inserted into the rat's right hindpaw. To synchronize EEG data with MRI scanning, analog outputs (5 volts) generated by a MRI console were digitized (16-bit resolution) as triggers to the EEG amplifiers and subsequently utilized for the off-line removal of scanning artifacts. The reference and ground electrodes (MR-compatible electrodes, NE-224S, Nihon Kohden, Tokyo, Japan) were subdermally inserted into the right and left ear-lobes, respectively.

### 3.5 MRI

All MRI data were acquired using a 7 T Bruker PharmaScan system (Bruker Biospin, Ettlingen, Germany) with a 38-mm-diameter bird-cage coil. Prior to all MRI experiments, global magnetic field shimming was first performed inside the core and later completed at the ROI using a point resolved spectroscopic protocol[107]. The line width (full width at half

maximum) at the end of the shimming procedure ranged from 15 to 20 Hz in the ROI (~ 300 μl).

### 3.5.1 EEG–fMRI experiment

#### 3.5.1.1 T1- and T2-weighted imaging

T1-weighted high-resolution images were obtained using 3D-RARE sequence with the following parameters: TR = 300 ms, TEeff = 8.5 ms, RARE factor = 4, SBW = 100 kHz, flip angle = 90 degree, FOV = 34 x 34 x 30 $mm^3$, matrix size = 272 x 272 x 60, voxel size = 125 x 125 x 500 $\mu m^3$, slice gap = 0 mm, and number of averages = 4. T1-weighted images were utilized for the identification of each electrode position and for the production of images of the rat brain and/or scalp surfaces. For T1-weighted image data processing and visualization, iMagic and Brainbow software (Neuronic S.A., Havana, Cuba) were used, respectively. T2-weighted high-resolution images were obtained using a 2D-RARE sequence with the following parameters: TR = 5800 ms, TEeff = 52.5 ms, RARE factor = 8, SBW = 62.5 kHz, flip angle = 90 degree, FOV = 25 x 14 $mm^2$, matrix size = 250 x 140, voxel size = 100 x 100 $\mu m^2$, number of slices = 27, slice thickness = 1.0 mm, slice gap = 0 mm, and number of averages = 8. T2-weighted images were utilized for GE-EPI image normalization to the rat brain atlas template[108]. Note that both T1- and T2-weighted imaging were performed under the condition in which the EEG mini-cap was disconnected from the amplifiers. The total scanning time for T1- and T2-weighted imaging was around 60 minutes and 13 minutes,

respectively.

#### 3.5.1.2 fMRI recording

For the phantom experiment, MRI scanning consisted of GE-EPI with the following parameters: TR = 2000 ms, TE = 15 ms, flip angle = 30 degree, FOV = 40 x 40 $mm^2$, matrix size = 100 x 100, voxel size = 400 x 400 $\mu m^2$, number of slices = 7, slice thickness = 1.5 mm, slice gap = 0 mm, number of volumes = 100 and dummy scans = 4. In the transmitter off and on mode, the SBWs were 500 kHz and 250 kHz, respectively. For the rat experiment, BOLD signals were obtained using GE-EPI with the following parameters: TR = 2000 ms, TE = 15 ms, SBW = 250 kHz, flip angle = 30 degree, FOV = 25 x 14 $mm^2$, matrix size = 125 x 70, voxel size = 200 x 200 $\mu m^2$, number of slices = 7, slice thickness = 1.5 mm, slice gap = 0 mm, number of volumes = 370, and dummy scans = 4. The total scanning time for the fMRI experiment was 12 minutes and 20 seconds.

#### 3.5.1.3 Relaxometry

T2* mappings were obtained using a MGE sequence with the following parameters: TR = 1500 ms, TE = 4.35, 9.35, 14.35, 19.35, 24.35, 29.35, 34.35, 39.35, 44.35, 49.35, 54.35, 59.35, 64.35, 69.35, 74.35, and 79.35 ms, flip angle = 30 degree, FOV = 32 x 32 $mm^2$, matrix size = 200 x 200, voxel size = 160 x 160 $\mu m^2$, number of slices = 7, slice thickness = 1.5 mm, slice gap = 0 mm, and number of averages = 4. The total scanning time for MGE was 15

minutes. MGE images were analyzed using SPM software (SPM5, Wellcome Department of Cognitive Neurology, London, UK) and a custom-written software in MATLAB (R2009b, MathWorks, Natiek, MA, USA). First, all MGE images for a particular rat were divided into three different conditions, i.e. with the EEG mini-cap (1), with the disconnected EEG mini-cap (2), without the EEG mini-cap (3). Second, for each condition, the 1st echo images (TE = 4.35) were aligned to the reference rat of that condition using the SPM coregistration algorithm. Third, T2* values were calculated for each rat by means of nonlinear least-squares of MR signal intensity (SI): $SI\ (k \cdot TE) = S_0 \exp\ (-k \cdot TE/T_2)$, where $k$ and $S_0$ represent the time samples and the signal intensity at time 0, respectively. Forth, the average and standard deviation of T2* values were calculated in each condition after normalizing all T2* images to the reference rat. Fifth, in order to focus on the target brain region, the whole brain was manually segmented, including both the gray and white matter, in the 1st echo image. A histogram was subsequently created for each rat.

#### 3.5.1.4 Transmitter attenuation

In all experiments, the RF transmitter pulse attenuation using the protocol provided by Bruker Biospin (AdjRefG, Paravision 5.0) was adjusted. This protocol is based on a 3-pulse $\alpha$ sequence;

$$\alpha - \frac{\mathrm{TE}}{2} - 2\alpha - \frac{\mathrm{TE}}{2} - \mathrm{SE} - \mathrm{TM} - \alpha - \frac{\mathrm{TE}}{2} - \mathrm{STE}$$

The sequence was performed with the following parameters: TE = 15 ms, SE (STE) is the

spin (stimulated) echo, TM = 45 ms is the filling period (i.e. mixing period for STE generation). A constant gradient that serves as slice selection was applied throughout the sequence in combination with the spoiling and frequency encoding gradient. The timing of the sequence ensured that a SE and STE signal would be centered in the acquisition period. The radio frequency waveform was fixed to a rectangular pulse. The adjustment algorithm varied the pulse amplitudes of both pulses and minimized the signal amplitude at the center of the STE slice profile (phase sensitive). The duration of the second RF pulse was twice the duration of the first one. Per default, the duration of the first pulse was 0.5 ms. The final attenuation in dB of the proton signal was stored.

### 3.5.2 MRI template experiment

#### 3.5.2.1 High resolution T2-weighted imaging

High resolution T2-weighted images were obtained using a respiratory-gated 2D TurboRARE sequence with fat suppression under the following parameters: TR = 10971 ms, TEeff = 30 ms, RARE factor = 4, SBW = 100 kHz, flip angle = 90 degree, FOV = 32 x 32 $mm^2$, matrix size = 256 x 256, voxel size = 125 x 125 $\mu m^2$, number of slices = 128, slice thickness = 0.3 mm, slice gap = 0 mm, and number of averages = 16. The total scanning time for T2-weighted imaging was around 3 hours, depending on the respiration rate of the rat.

#### 3.5.2.2 Low resolution T2-weighted imaging

In order to perform the necessary image processing (spatial registration and tissue segmentation), both the fMRI and DTI experiments were accompanied with a low resolution T2 MRI with exactly the same parameters as the high quality one; excepting for the number of averages (10), the slice thickness (0.5 mm), and the number of slices (54). These parameters were chosen to reduce the scanning time of this image to around 50 minutes, making possible its inclusion in the fMRI and DTI experiments.

### 3.6 Forepaw/hindpaw electrical stimulation

A block-design paradigm consisting of ten blocks was employed in which each block, comprising 30 s forepaw/hindpaw stimulation followed by a 40 s resting condition. To produce the electrical pulses (3 Hz, 3.0 mA, and 0.3 ms width), a generator (SEN-3401, Nihon Kohden, Tokyo, Japan) and an isolator (SS-203J, Nihon Kohden, Tokyo, Japan) were utilized.

### 3.7 Data analysis

#### 3.7.1 EEG–fMRI experiment

##### 3.7.1.1 EEG data analysis

EEG data analysis was carried out using custom-written software in MATLAB. The templates of the scanning artifact were computed based on PCA. In the rat experimental paradigm, the number of fMRI volumes and slices is 370 and 7, respectively, which resulted

in 2590 indices of scanning triggers. First, EEG data was segmented into 2590 epochs ranging from the scanning onset (0 s) to a duration of 0.25 s and the mean change of each epoch was subtracted (baseline correction). Second, the PCs were computed using all epochs and the first 3 PCs were used to produce the scanning artifact template. This template was eventually subtracted from the EEG data for each channel. Third, the corrected EEG data was band-pass filtered (6th order Butterworth filter, 0.5–70 Hz) and down-sampled to 500 Hz. Forth, the mean-evoked somatosensory potential for each stimulation condition was computed from 900 individual evoked potentials. Finally, Euclidean distance and Pearson's correlation coefficients were computed for pair-based comparisons

**3.7.1.2 fMRI data analysis**

fMRI data analysis was carried out using SPM5 and custom-written software in MATLAB. The preprocessing of fMRI images was performed as follows. First, the adjustments of acquisition timing across slices and the motion artifact corrections of the individual rat's brains were performed. Second, fMRI images were co-registered to the T2-weighted anatomical reference which was normalized beforehand to rat's atlas template[108)]. Finally, spatial smoothing was performed using a Gaussian kernel of 0.8 mm full width at half maximum. Single-subject analysis of the preprocessed fMRI data was performed in SPM5 with a critical T-value for each voxel ($p < 0.05$, FWE corrected). To further evaluate the fMRI results, an average time course within the spherical ROI (0.6 mm radius) was extracted and

centered among the highest T-scores. The time courses of the fMRI data were low-pass filtered (6th order Butterworth filter, < 0.1 Hz) and averaged.

### 3.7.2 MRI template experiment

#### 3.7.2.1 Digitalization of the P&W atlas

The 6th version of the P&W stereotaxic atlas was originally provided in PDF format[109]. A total of 48 cortical structures on each side of the brain (total: 96) were manually delineated with Adobe Illustrator in the coronal slices of this PDF book. A BITMAP image of each coronal slice containing a set of closed and filled contours of the cortical structures was obtained. Ad-hoc software was developed to align and interpolate these bitmaps to produce a digital volume in the P&W space (isotropic voxel size of 0.12 mm). The image extends from −8.64 mm to 8.64 mm left to right, from −15.96 mm to 7.56 mm caudal to ventral and from −14.16 mm to 1.8 mm ventral to dorsal. The origin of this coordinate system was located in the Bregma. A binary mask including all voxels of the brain was created and the surface enclosing this mask was extracted. In the same way, the mask and the corresponding enclosing surface for the voxels belonging only to the cortex was created. Both pairs of masks and surfaces were used to refine the registration between the MRIs and the P&W space.

#### 3.7.2.2 Construction of the average template image

All high resolution T2 MRIs were registered to the 6th version of the P&W space using

a “nonlinear” ATPS registration method[110]. A total of 36 points, i.e. “landmarks”, were defined in the P&W space (target) and their corresponding pairs were manually located in the individual MRIs (source). The landmarks were located using T2-CARB software. The following outlines the steps for the construction of the average template image.

1. The four landmarks described in Table 3.3 were identified.
2. The 36 landmarks described in Table 3.4 were identified.
3. A binary brain mask was extracted using a semi-automatic segmentation method[111].
4. The mask was transformed by means of dilations and erosions, and a final sinc smoothing to remove isolated holes and severe irregularities in the outer boundary.
5. A set of about 700 regularly spaced points belonging to the mask were randomly chosen. A second set of corresponding points in the digitalized P&W atlas were assessed allowing for a final refinement of the ATPS registration.
6. The MRI image was spatially normalized to the atlas space using the affine + ATPS (36 landmarks +700 points) concatenated transformation.
7. The average template image was computed and the left and right hemispheres were averaged to create a symmetric image like the P&W atlas. These constitute the average MRI and brain only MRI templates of the template.

#### 3.7.2.3 SPM normalization of low resolution MRI images

The low resolution MRI was normalized to the template and linearly coregistered to the first scan of the functional MRI experiment using SPM5. After slice timing and inter-scan motion correction, the fMRIs were normalized to the P&W space with the SPM5 normalization transformation of the coregistered low resolution MRI. Spatial smoothing was performed using a Gaussian kernel of 0.8 mm full width at half maximum. Single-subject analysis was performed with a critical T-value for each voxel calculated for a significance level of $p < 0.05$ (FWE corrected). The significant activations were overlaid on the digitalized P&W atlas.

# SECTION 4 RESULTS

## 4.1 The feasibility of the EEG–fMRI experiment

### 4.1.1 Weisskoff's test in phantom

To evaluate the interference of the EEG mini-cap on MRI signal stability, "Weisskoff test"[104] using a pre-established suitable phantom was employed (Figure 4.1). The averaged T2 value in the phantom was 124 ± 1.9 ms, which is comparable to that observed in the gray matter of humans[112]. In the test, the time-courses of MRI signals are primarily de-trended and the residuals are used to calculate global standard deviation. Theoretically, the standard deviation should linearly decrease when enlarging the ROI. For each ROI, any difference between the theoretical and measured standard deviations is attributable to extra temporal fluctuations in the MRI image. The point from which these two curves begin to deviate is named the RDC. To quantify the effect of the EEG mini-cap on the MRI receiver coil, first the test with the transmitter-off condition (i.e. there is no RF excitation pulse) was performed. As shown in these panels, in the absence of the EEG mini-cap, RDC was 16.9 voxels and in the presence of the EEG mini-cap, RDC was 8.9 voxels. The platinum electrodes, EEG paste, skin and wire loops may form RF antennas that pick up external RF energy[113]. This could be a possible mechanism behind the interference from the EEG mini-cap that results in a RDC drop during the transmitter-off condition. However, in the transmitter-on condition, where a MRI phantom signal is expected, the RDC in both cases was around 2. This implies the

nonexistence of extra interference from the EEG mini-cap for standard GE-EPI protocols. Therefore, the EEG mini-cap has no significant effect on the temporal fMRI signals.

### 4.1.2 Magnetic field disturbance

The presence of a dense array of platinum electrodes, the EEG paste, the conducting copper leads, and the plastic basement could cause MRI signal degradation due to magnetic susceptibility effects. Examples of such degradation are signal drop-out, image distortion and the perturbation of radio frequency fields[74]. To compare the susceptibility effects of the EEG mini-cap on the rat's brain, T2* mapping was evaluated in three different conditions: 1) with the EEG mini-cap, 2) with the EEG mini-cap disconnected from the amplifiers and 3) without the EEG mini-cap. Conditions (1) and (2) were used to determine the effects on the MRI image of the materials utilized to build the EEG mini-cap, while conditions (2) and (3) were useful to isolate those undesirable effects produced by the EEG recording system.

Figure 4.2 shows the T2* mappings (the average and standard deviation, $n = 6$) from similar coronal slices acquired in each of three conditions. While the localized field inhomogeneities resulting from the EEG mini-cap were not visible, global field inhomogeneities were observed in the T2* mapping for all conditions. The global inhomogeneities were attributable to the characteristics of the MRI hardware system.

Figure 4.3 shows the histogram of T2* values obtained from the segmented rat brain, including both the gray and white matter. The distributions of T2* [conditions: (1) 26.0 ± 10.1,

(2) 25.2 ± 10.1, (3); 25.9 ± 9.9] were similar to those reported in a recent study[114]. Using the one-sample Jarque–Bera test[115], the distributions of the T2* in the segmented brain were confirmed as Gaussians (i.e. normal distributions) ($p > 0.01$) with comparable means and standard deviations. In order to verify if any particular TE was preferentially affected, a two-sample T-test was used for pair-based comparisons of these three different conditions.

Figure 4.4 shows the p-score of each T2* sampling point. If the p-score is higher, the two-samples are almost identical. This analysis revealed that there are three TE clusters with high p-values. In the fMRI experiment, GE-EPI sequences with TE = 15 ms were employed in one of the highest p-value clusters. Therefore, extra inhomogeneities in the magnetic field were not distinguishable in the rat brain in the presence of the EEG mini-cap for the GE-EPI sequence used in this paper.

MRI utilizes a highly-uniform magnetic field, which is perturbed by the presence of any material with a magnetic susceptibility $\chi$. The degree of disturbance depends on the strength of the static magnetic field $B_0$ and the magnetic susceptibility of the material ($B_0 = \chi B_0$). Therefore, the material and size of the EEG electrode, as well as the conductive EEG paste/gel, must be carefully-selected[51]. In this study, platinum wires ($\chi = \sim 200$) were utilized in a 7 T MRI magnet. The diameter and length of the metal material were minimized as much as possible using the proposed EEG electrode system. In addition, to avoid close proximity to

the brain tissue, the EEG mini-cap was prepared to ensure a distance of 1 mm between the platinum wire and the tip of the tube.

### 4.1.3 Temperature monitoring

In this study, GE-EPI sequences were employed. These are known to have low-SAR compared with conventional spin-echo sequences because only a single RF pulse is required per imaging slice (e.g. 0.08 ± 0.01 W/kg[116]). However, the placement of conductive EEG electrodes and leads inside the MRI scanner is problematic since the induced currents in the electrodes are much greater than those induced in the biological tissues[49]. To evaluate the heating effects of the EEG mini-cap on rats, the rat's ear temperature was observed under different conditions. Figure 4.5 shows the time-course of the temperature changes under the GE-EPI sequences. The maximum temperature changes were 0.28 ± 0.04 °C (without the EEG mini-cap) and 0.38 ± 0.06 °C (with the connected EEG mini-cap), which are consistent with those changes observed in similar experimental set-ups in sheep (0.4 °C)[117]. The changes also comply with the safety limits (< 1 °C) recommended by the International Electrotechnical Commission[118]. Therefore, the thermal effects of the EEG mini-cap can be disregarded. Note that further temperature monitoring needs to be evaluated on a case-by-case basis since SAR depends on the utilized MRI sequence, coil type, and magnetic field strength, as well as the characteristics of EEG electrodes and leads[119) 106].

### 4.1.4 fMRI signal quality

The RF transmitter pulse attenuation in the presence and absence of the EEG mini-cap was evaluated (Table 4.1). The attenuation was relatively similar in both conditions (averaged values were around 27 dB).

Figure 4.6 shows the fMRI signal of a single rat after normalization to the rat atlas template. The maximum T-score of the fMRI signal (cross-hair pointer) was located in the primary somatosensory cortex for all rats and across all conditions (Table 4.2). Note that the brain atlas template is in the standard coordinate system[120].

The temporal dynamics of the fMRI signals were additionally calculated inside a spherical ROI (Figure 4.7). Although the amplitudes of fMRI signal changes were almost comparable in the three different conditions, the standard deviations were slightly different with more variability when the EEG mini-cap was inside the scanner and connected to the amplifiers. This result may be associated with the stability of the receiver coil in the presence of the EEG mini-cap, as demonstrated in the phantom experiment (Figure 4.1).

Although the EEG mini-cap seemed to compromise the temporal stability of the MRI receiver coil in the transmitter-off condition, the quality of the signal was not impaired when the transmitter was “on”. Note the differences in the RDC for the transmitter “off” and “on” conditions. This impairment could be due to the fact that not only $B_0$, but also the excited magnetic field $B_1$ created by the transmitter coil, contributed to the final observable MRI signal[121]. However, temporal instability caused by fluctuations/heterogeneities in both

magnetic field $B_0$ and $B_1$ were independent of the presence of the EEG mini-cap. The time courses and activated areas in the fMRI signals were comparable in all conditions, a fact that could be explained for the following reasons: 1) the EEG mini-cap introduced no significant inhomogeneities in the magnetic field, 2) an automatic adjustment of the transmitter pulse attenuation was good enough to compensate any instability and/or disturbance of the magnetic field. fMRI results were also found to be reproductions of those obtained in previous studies for similar experimental paradigms and rat strains[122) 123) 107)].

### 4.1.5 EEG scanning artifacts

Two types of artifacts in the electrophysiological recordings originate specifically from the MRI scanner. They are related to 1) the scanning process (*scanning artifact*) and 2) cardiac pulsation (*ballisto-cardiogram artifact*). The scanning artifact is usually the largest in amplitude (in the order of mV) and the most stable over time[53)]. This artifact is generated by time-varying electromagnetic fields through any closed loop in the hardware for EEG recording. These unavoidable closed loops are formed, for instance, by the wiring used to connect the electrodes and the EEG amplifiers. The ballisto-cardiogram artifact is thought to result from heart beat related movements of the head[52)], but the biophysical mechanisms underlying its origin are still unclear[17) 124)]. In this study, EEG signals in rats were obscured by MRI scanning artifacts in a similar way to those signals reported in humans[68)] (Figure 4.8.A). However, the amplitude of this type of artifact was smaller (i.e. peak-to-peak amplitude) in rat

5 mV than in human 14 mV. The most common approach used these days to correct the imaging artifact is to generate a template (Figure 4.8.C) of its gradient-induced waveform and to subtract this template from the EEG raw signals. This template depends on the TE and TR used in the experimental protocol. By using a PCA-based subtraction method, which is combined with a data down-sampling of 500 Hz, the EEG signals were cleaned from these scanning artifacts (Figure 4.8.B). In contrast, the ballisto-cardiogram artifacts were not significant in the rat's EEG (Figure 4.8.B), which is consistent with the results mentioned in the literature[125]. Therefore, in the current study, no method for correcting the ballisto-cardiogram artifacts was applied.

### 4.1.6 EEG signal quality

Figure 4.9.A shows the grand average of ERP. The temporal dynamics of the EEG signals evoked by the electrical forepaw stimulation are consistent with those reported in the literature[122) 123) 126)]. The Euclidean distance (Figure 4.9.B) and the Pearson's correlation coefficients (Figure 4.9.C) in three different experimental situations were evaluated: 1) outside the MRI scanner, 2) inside the MRI scanner without MRI scanning and 3) inside the MRI scanner with MRI scanning. Situations (1) and (2) were used to evaluate the effects of ballisto-cardiogram artifacts, while situations (1) and (3) were used to evaluate the effects of both scanning and ballisto-cardiogram artifacts after correcting the former. From this analysis, the signal-loss caused by the ballisto-cardiogram and the scanning artifacts in ERP were

comparably negligible (< 5% in the peak amplitude). The subtraction method established for humans was permitted for correcting these types of artifacts in rats as well. Consequently, it can be concluded that there were no significant differences in the grand average of EEG recordings after removing the scanning artifacts for each quantitative channel compared to those obtained without scanning and outside the scanner. The waveform of this grand average was consistent with others obtained in previous experiments[123) 126)].

### 4.1.7 Evoked potential mapping

Figure 4.10.A shows the grand average of the somatosensory ERP for all EEG electrodes obtained simultaneously with fMRI signals from a single rat. Figure 4.10.B shows the topographic maps of the somatosensory ERP on the rat scalp surface. These data suggest that forepaw stimulation evokes spatiotemporal patterns of brain activity which utterly correspond with the idea of largely distributed neuronal networks underlying somatosensory processing in rats [voltage sensitive dyes – Ferezou et al., (2007)[127)]; fMRI – de Celis Alonso et al., (2008)[128)]].

## 4.2 The MRI template construction

### 4.2.1 Average template image

Figure 4.11 depicts the left hemisphere of the symmetrically averaged T2 MRI template of the 30 Wistar rats in the 6th edition of the P&W space[109)]. The digitalized P&W atlas is

overlaid on this image and the original contour-based image from the P&W PDF is shown in the right hemisphere for comparison. Regarding the average template, firstly, this template has some advantages to the template of Schweinhardt et al., (2003)[108], which is based on MRIs from an MR system with a lower main magnetic field strength (4.7 T) and less spatial resolution (117 x 117 x 500 $\mu m^3$). Second, compared to Lu et al., (2010)[129], a preliminary evaluation by visual inspection demonstrates the ability of the ATPS method to satisfactorily warp the individual MRIs to the atlas space, giving special attention to the gray/white matter interface.

### 4.2.2 SPM normalization of low resolution MRI

A spatially normalized low resolution MRI is shown together with the average template in Figure 4.12 for three different orthogonal views. It is important to note that for a correct spatial SPM5 normalization of the individual MRI, a rigid orientation is first mandatory, i.e. the rat head must be oriented to have the same coordinate convention as the atlas space (X: mediolateral, Y: caudorostral and Z: ventrodorsal), and the origin must be as close to Bregma as possible. This procedure has been widely applied in human head MRI spatial normalization, namely in the so-called anterior and posterior commisural alignment.

### 4.2.3 ROI-based anatomical interpretation of fMRI

Figures 4.13 and 4.14 show, in orthogonal views on the average template, the fMRI activations caused by forepaw and hindpaw stimulations, respectively. As expected, they are located within the contralateral forelimb and hindlimb of the somatosensory cortex, respectively[103]. To evaluate the accuracy of this localization, the percent of voxels within the corresponding anatomical region, which have a T-value above 6, 7, 8 and 9, is calculated for each stimulus. These values are [74.0%, 77.1%, 79.2%, 82.1%] for the left forepaw, [87.7%, 94.4%, 97.7, 100.0] for the right forepaw, [75.2%, 88.0%, 97.0, 100.0%] for the left hindpaw, and [60.7%, 75.7%, 92.6%, 0% (no voxel having T-value>9)] for the right hindpaw. This demonstrates that the center and most parts of the significantly activated regions are within the corresponding expected anatomical areas. fMRI forepaw results resemble those obtained in Schweinhardt et al., (2003)[108] and Lu et al., (2010)[129], with the advantage that it is possible to quantify the number of activated voxels within the corresponding cortical structure.

# SECTION 5 DISCUSSIONS

The author has, for the first time in the world, introduced both a new EEG mini-cap and a protocol to simultaneously obtain whole scalp EEG signals and fMRI signals in small animals. The quality and reproducibility of both EEG and fMRI signals were demonstrated using a conventional forepaw stimulation paradigm ($n$ = 5). The proposed methodology provides a number of distinct advantages over existing techniques: for example, fewer magnetic field interferences, greater reduction of scanning artifacts in the EEG signal, a broad array of EEG electrodes, and reproducible EEG and fMRI signals. Additionally, the new T2 MRI template from Wistar rats ($n$ =30) and the 96 digitized cortical structures of the P&W atlas have been provided so that a statistical tool for rat fMRI having a wide variety of applications, e.g. ROI-based connectivity analysis, could be provided. These methodologies could be directly generalized to other rat types and ages, as well as to mice. However, to further improve the study and technical aspects of the proposed methodology, several limitations of both the EEG–fMRI and MRI templates are described below.

### 5.1 Limitations of the EEG–fMRI study

**General view**: fMRI can provide excellent spatial resolutions as high as 100 μm, but fMRI is temporally limited to a period of several seconds to several minutes. In contrast, EEG has superior temporal resolution compared to fMRI which allows studies of the dynamics of neural networks that occur on the order milliseconds. Unfortunately, the spatial resolution of

EEG does not match that of fMRI due to its limited number of spatial measurements and the ill-posed nature of EEG inverse problems[130]. Effective combinations of the two different kinds of modalities might provide new insight that could not be achieved with either modality alone. However, the limitation is actually that the complexity of the brain, with its many interacting elements, makes it extremely difficult to say whether or not two findings obtained using methods with different spatial and temporal features do or do not agree. This issue underlies many challenges and has been a source of much debate because there is no solid understanding of the neural substrates of fMRI activations, specific EEG components, nor the effects of a focal lesion on how a neural network behaves. For example, Vitacco et al., (2002)[131] investigated whether or not the brain regions that show large activations by fMRI also show large LORETA values using a semantic monitoring task. To deal with the different spatiotemporal resolutions of the two methods, they averaged their LORETA values across all temporal epochs and attempted to identify each LORETA local maximum with its nearest fMRI local maximum in a statistically meaningful manner. They found that this could be done for group mean data, however on an individual basis, only half of the subjects showed a significant correspondence between the fMRI and LORETA patterns. Therefore, one needs to be very careful when combining two or more different spatio-temporal neuroimaging modalities. Several neuroscientists have proposed solutions to overcome these EEG–fMRI limitations (e.g. biophysical model[17) 21)], data-driven multiway Partial Least-Squares[6) 132)]).

**In this study**: Using the two cylindrical plastic tubes in which a platinum wire was immersed in a mixture of EEG paste and saline solution[133)] in the inner tube, the feasibility of simultaneous EEG–fMRI recording in small animals was proven**.** However, this study still has several limitations. Firstly, the EEG mini-cap does not cover the entire brain (Figure 4.10). For example, the olfactory bulb, cerebellum and lateral side of the cerebral cortex (e.g. secondary somatosensory cortex, auditory cortex) are undesirably far from the EEG electrodes because each electrode needs to be allocated perpendicularly to the scalp. Unfortunately, due to the limited available surface area of the scalp, the structure of the rat head does not allow each electrode to be allocated at the correct angle. This leads to the disadvantages of EEG source localization with ipsi-lateral activity after 24 ms in Figure 4.10 as an example. One needs to carefully consider the EEG current source since it seems to be difficult to distinguish meaningful neuronal activity (via the corpus callosum) from mere compensatory isoelectrical potentials due to the large negativity in the contra-lateral cortex. Secondly, contamination of EEG recordings from scanning and ballisto-cardiogram artifacts constitutes one of the most critical problems in EEG–fMRI concurrent experiments. The scanning artifacts are very reproducible across consecutive volume acquisitions and, therefore, they can be satisfactorily removed from the raw data by subtracting an artifact template (Figure 4.8) (note: for such purpose, the exact scanning trigger positions and a high-sampling rate of EEG data are required). Ballisto-cardiogram artifacts have been found to be

neglectable in event-related paradigms in rats. However, it should be noted that, for a spontaneous EEG–fMRI data analysis, a correction method for the ballisto-cardiogram artifacts need to be developed suitably[134].

### 5.2 Advances and limitations of the MRI template

The author constructed a new MRI template set of Wistar rats in the 6th and last version of the P&W atlas space comprising: 1) an average of 30 T2-weighted MRIs and 2) an image with 96 digitalized cortical structures of the P&W atlas. In contrast to previous templates, I established a nonlinear spatial correspondence between the individual MRIs and the atlas space by means of the ATPS registration method, based on 36 landmarks carefully selected in both spaces. By visually comparing either individual or average template MRI with the P&W atlas, an improvement can be seen in the correspondence between the two when compared with correspondence seen in the work of Schweinhardt et al., (2003)[108], Schwarz et al., (2006)[135], and Lu et al., (2010)[129]. The fMRI findings were enriched by accurately locating activations associated with the forepaw and hindpaw in both hemispheres in the expected anatomical regions of the P&W atlas. Note that hindpaw stimulation was not tested previously, probably due to difficulty in obtaining a robust and distinguishable activation. As in Schwarz et al., (2006)[135], a quantitative evaluation of the fMRI results was possible due to the atlas digitalization. The author perceives a future interest in using this ROI-based technique to probe the anatomical substrates of various fMRI-proven connections between either ipsilateral

or contralateral areas[98) 136) 137) 138)]. The feasibility of combining different neuroimaging techniques to assess connectivity, such as fMRI, DTI, and the recent "morphological connectivity", which is based in either volume or area ROI/ROI correlations[139)], opens a wide window for understanding rat brain anatomical and functional networking. However, the digitalized cortical structures are restricted in the cerebral cortex in the P&W atlas (Figure 4.11). Therefore, one can't extend the MRI analysis to the white matter cortex (e.g. limbic system, cerebellum). This will be upgraded using semi-automatic segmentation and digitalization of the BITMAP images of the P&W book in the near future.

### 5.3 Examples of future studies

To exemplify the proposed methodology in the near future, examples of possible neuroscientific studies in which one can maximize the potential of the proposed technologies is discussed below. Some of them have already been employed in the author's laboratory and the others are future perspectives.

#### 5.3.1 Large-scale dynamics in the forepaw stimulation paradigm

In previous studies using EEG and fMRI simultaneous recordings in small animals (Table 1.4), just a few electrodes were utilized. For example, to study the somatosensory system in rats, a previous study performed EEG–fMRI simultaneous recordings with the electrodes placed on the somatosensory cortices during forepaw stimulation[66)]. Using a few

electrodes seems to be suitable for a pre-defined stimulus paradigm, such as electrical forepaw stimulation, due to its predictable evoked response in the corresponding cortices. It is also suitable for studying particular brain regions. However, this seems to be inconvenient when one focuses on large-scale changes in neuronal activity. For example, in epilepsy, the exact position and onset of seizures are inherently unpredictable. Therefore, a large number of EEG recording sites are required to determine "*when*" and "*where*" the seizure originated. Increasing the number of recording electrodes has added to the potential for improving source localization[63]. Devor et al. (2008)[140] have found a local decoupling between neuronal activity and blood flow in the ipsi-lateral somatosensory cortex of rats, while the contra-lateral somatosensory cortex showed a typical blood flow response. They observed that hemodynamic responses decrease in the ipsi-lateral, and this effect was associated with arteriolar vasoconstriction in the presence of increased spiking activity. A critical issue in that study is the position from where electrophysiological data is observed. Inaccurate electrode insertion in the cortex through the craniotomy could lead to the wrong understanding of the electrophysiological data. In such cases, one can benefit from a high-dense array of EEG electrodes placed over the entire skull/scalp area and could therefore characterize functional connectivity patterns between different cortical areas. These advantages could also help in the validation of the previous results by Ogawa et al. (2000)[102] that reported the dependency of the inhibitory delays in bilateral forepaw stimulation paradigm on hemodynamic response. By

combining large scale EEG data reflecting activity from all cortical areas and the fMRI signal, one can disentangle the spatial-dependent relationships between neuronal activity and associated hemodynamic responses. It should be noted that detailed configurations of neuronal activity can be estimated using a sophisticated EEG inverse solution arising from large scale brain dynamics.

### 5.3.2 Combination of EEG–fMRI and physiological monitoring

Figure 5.1 shows simultaneous EEG and fMRI data (from a single rat). Figure 5.1.B shows the fMRI activation map for the on-off estimation contrast. Figure 5.1.C shows the time course of single trial EEG recordings and the fMRI signal (inside a spherical ROI, materials and methods). One can appreciate event-related EEG responses even from single trials, which illustrate the good signal-to-noise ratio achieved by the proposed experimental methodology.

One of distinct advantages in animal models is that they allow the investigator to perform invasive physiological monitoring in the MRI scanner. Table 5.1 summarizes the physiological variables of Wistar rats obtained during simultaneous EEG and fMRI experiments ($n$ = 5). Since both EEG and fMRI signals are sensitive to physiological variables[141) 98) 80)], the investigator needs to carefully control such parameters to maintain them in an acceptable physiological range. This is especially important when the investigator performs either physiological or pharmacological interventions in experimental animal

models. To properly interpret these findings, the investigator needs to discuss the plausible mechanisms with the properly-obtained physiological variables.

More importantly, some investigators have utilized the observed physiological variable of biophysical models to relate a functional activation (in both neuronal and hemodynamic reflections) to the physiological states [$O_2$ dynamics: Boas et al., (2008)[142]; $CO_2$ kinetics: Yücel et al., (2009)[143]]. In this sense, the combination of EEG–fMRI and concurrent physiological monitoring are ideal and can largely contribute to the development of such important biophysical modeling.

### 5.3.3 Pharmacological approach to studying neurovascular coupling

The current understanding suggests that neuronal and/or astroglial signals transduce changes in neuronal activity into an integrated vascular response which results in a regional increase of blood flow within the activated area (i.e. functional hyperemia). However, the physiological mechanism of neurovascular coupling is still controversial and unclear[37]. In particular, the time dependency and relative contribution of each phasic/tonic pathway has not been described yet in the literature[144) 97]. This concept is schematically illustrated in Figure 5.2.

To elucidate these mechanisms, an appropriate animal model is needed to perform pharmacological/physiological interventions during electrophysiological (i.e. an indicator of neuronal activity) and fMRI (an indicator of hemodynamic responses) recordings [for the

pharmacological protocols, nNOS: Stefanovic et al., (2007)[122]; COX-2: Bakaloba et al., (2002)[145]; mGluR5: Wang et al., (2006)[42]; $cPLA_2$: Takano et al., (2006)[41]; COX-1: Niwa et al., (2001)[146]]. Ultimately, the methodology should use concurrent observations, since the physiological state of the anesthetized animals will change dramatically as time elapses after the initiation of anesthesia[141) 81)]. This may lead to side effects in EEG and fMRI data.

### 5.3.4 The use of an animal disease model

One of the ultimate goals among numerous applications is to study the pathological nature related to brain diseases such as epilepsia, dementia, and ischemia. These days, a number of animal disease models have been developed and utilized in MRI studies. Table 5.3 summarizes the study of animal disease models, demonstrating their feasibility in a high-field MR scanner and exemplifying the value of MRI techniques. Simultaneous EEG and fMRI recording in small animals will also be appreciated as an essential technique since it is unique and could provide greater spatial and temporal signatures in manners non-invasive measurement.

In parallel with these perspectives, phMRI, used to investigate brain function in response to pharmacological investigation in rats and humans, is getting much attention in academia and also the pharmaceutical industry since it may provide drug screening platform using healthy and pathological animal models. Taking into account such forward movement in the neuroimaging society, the proposed methodology (EEG–fMRI in small animals) could

play a central role in neuroscience and psychopharmacological disciplines in the near future.

# SECTION 6 CONCLUSIONS

In this work, 1) the author introduced both a new EEG mini-cap and a protocol to obtain whole scalp EEG recordings simultaneously with 7 T fMRI signals in small animals. The quality and reproducibility of both EEG and fMRI signals were demonstrated using a conventional forepaw stimulation paradigm in Wistar rats. Based on this quantitative analysis, the author concludes that simultaneous EEG–fMRI recordings are achievable in small animals without significant signal loss; 2) the author constructed a new MRI template set of Wistar rats in the last version of the P&W atlas space comprising an average of 30 T2-weighted MRIs and an image with 96 digitalized cortical structures of the P&W atlas. The author exemplified the versatility of the mini-cap's application in a forepaw/hindpaw stimulation paradigm and confirmed fMRI localization by ROI-based anatomical quantifications. Through experimental manipulations with different levels of invasiveness, i.e. the contemporary transgenic models and advanced drug administration protocols in small animals, the proposed methodologies were shown to be potentially valuable for studying the mechanisms of healthy brains (e.g. neuron-to-vascular coupling), as well as those associated with pathological states (e.g. epilepsy, neurodegenerative diseases). Presumably, the proposed methodology (i.e. EEG–fMRI and MRI template in small animals) could also be applied to drug screening tests in the pharmaceutical companies, and expectantly it will be remarkable as a future experimental platform in both academic and industrial laboratories.

# SECTION 7 ACKNOWLEDGEMENTS

It is a great pleasure to thank all of the people who have helped and encouraged me for the period of my doctoral study. I especially would like to thank my senior supervisor, Prof. Ryuta Kawashima, for his mentorship and all-out support for the past three years. I am always impressed by his scientific acumen and charismatic leadership, and am grateful for the many opportunities to learn and study that he has offered me in his laboratory. I am quite sure that my research goals would not have been accomplished without his contributions.

I would like to deeply thank my direct supervisor, Prof. Jorge J. Riera, for his supervision, guidance, and encouragement during my doctoral study. When I first came to his laboratory he kindly accepted and welcomed me to my current scientific field. I am always motivated by his enthusiasm in research and encouraged by his courteous considerations. I have benefited much from many talks with him, both academically and personally. His mentorship is sometimes strict, yet sometimes relaxed and jovial. He certainly is a great example of how I would like to work in this scientific field in the future.

I also devote my gratitude to all members of the Department of Functional Brain Imaging, especially to the NMD members, including Prof. Tadao Miyamoto, Dr. Takakuni Goto, Dr. Moataz Mekawy, Ms. Risa Haga, Ms. Yuka Konno, Mr. Takeshi Ogawa, and Mr. Hiroi Nonaka for their encouragements and support in my research and study. Moreover, I give my sincere thanks to Ms. Sarah Michael, for her clear-cut English corrections of my

scientific manuscripts and her obliging weekly English lessons. I would also like to thank some members of other laboratories at Tohoku University, including Prof. Hiroaki Shimokawa, Dr. Hideaki Suzuki, Dr. Toshiki Endo, Dr. Misaki Kohama, Dr. Atsushi Saito, and Dr. Miho Matsumata for their fruitful collaborations.

I am deeply grateful for the basic MRI training I received at the University of Hong Kong (Prof. Ed X. Wu) (November 2008), Max-Plank-Institute (Dr. Kâmil Uludağ) (December 2008) and the Montreal Neurological Institute (Prof. Alan C. Evans) (August 2009). The friendship and joyful discussions I've shared with Dr. Kevin C. Chan and Dr. Matthew M. Cheung (University of Hong Kong); Dr. Baris Yesilyurt, Dr. Mustafa Cavusoglu, and Dr. Hannes M. Wiesner (Max-Plank-Institute); Dr. Maxime Boucher and Dr. François Hebert (Montreal Neurological Institute) and the other people in their institutes whom I greatly value. I extend my gratitude to Dr. Pedro A. Valdes-Hernandez, Dr. Eduardo Aubert-Vazquez, Dr. Yasser Iturria-Medina, Dr. Jorge Bosch-Bayard, and Prof. Pedro A. Valdes-Sosa (Cuban Neuroscience Center), as well as Dr. Benjamin Thyreau (Neurospin) and Dr. Xiaohong Wan (RIKEN) for their tremendous support in EEG and/or MRI data analysis. I also thank Dr. Robert Stoermer and Dr. Ingmar Gutberlet (Brain Products) for their helpful comments.

Last, but not the least, I would like to thank my wife, Mrs. Yuki Sumiyoshi, and my parents for their tremendous support for the course of my 3-year doctoral study.

# SECTION 8 REFERENCES

## 8.1 Bibliography


1. Friston KJ: Modalities, modes, and models in functional neuroimaging. Science 326:399-403, 2009
2. Raichle ME: A brief history of human brain mapping. Trends Neurosci 32:118-126, 2009
3. Bandettini PA: What's new in neuroimaging methods? Ann N Y Acad Sci 1156:260-293, 2009
4. Lemieux L, Krakow K, Fish DR: Comparison of spike-triggered functional MRI BOLD activation and EEG dipole model localization. Neuroimage 14:1097-1104, 2001
5. Mulert C, Jäger L, Schmitt R, et al: Integration of fMRI and simultaneous EEG: towards a comprehensive understanding of localization and time-course of brain activity in target detection. Neuroimage 22:83-94, 2004
6. Martínez-Montes E, Valdés-Sosa PA, Miwakeichi F, et al: Concurrent EEG/fMRI analysis by multiway Partial Least Squares. Neuroimage 22:1023-1034, 2004
7. Valdes-Sosa PA, Sanchez-Bornot JM, Sotero RC, et al: Model driven EEG/fMRI fusion of brain oscillations. Hum Brain Mapp 30:2701-2721, 2009
8. Heinze HJ, Mangun GR, Burchert W, et al: Combined spatial and temporal imaging of brain activity during visual selective attention in humans. Nature 372:543-546, 1994
9. Liu AK, Belliveau JW, Dale AM: Spatiotemporal imaging of human brain activity using functional MRI constrained magnetoencephalography data: Monte Carlo simulations. Proc Natl Acad Sci U S A 95:8945-8950, 1998
10. Debener S, Ullsperger M, Siegel M, et al: Trial-by-trial coupling of concurrent electroencephalogram and functional magnetic resonance imaging identifies the dynamics of performance monitoring. J Neurosci 25:11730-11737, 2005
11. Warach S, Ives JR, Schlaug G, et al: EEG-triggered echo-planar functional MRI in epilepsy. Neurology 47:89-93, 1996
12. Krakow K, Woermann FG, Symms MR, et al: EEG-triggered functional MRI of interictal epileptiform activity in patients with partial seizures. Brain 122:1679-1688, 1999
13. Goldman RI, Stern JM, Engel J, et al: Simultaneous EEG and fMRI of the alpha rhythm. Neuroreport 13:2487-92, 2002
14. Laufs H, Kleinschmidt A, Beyerle A, et al: EEG-correlated fMRI of human alpha activity. Neuroimage 19:1463-1476, 2003
15. Moosmann M, Ritter P, Krastel I, et al: Correlates of alpha rhythm in functional magnetic resonance imaging and near infrared spectroscopy. Neuroimage 20:145-158,

2003
16. Schabus M, Dang-Vu TT, Albouy G, et al: Hemodynamic cerebral correlates of sleep spindles during human non-rapid eye movement sleep. Proc Natl Acad Sci U S A 104:13164-13169, 2007
17. Riera JJ, Aubert E, Iwata K, et al: Fusing EEG and fMRI based on a bottom-up model: inferring activation and effective connectivity in neural masses. Philos Trans R Soc Lond B Biol Sci 360:1025-1041, 2005
18. Riera JJ, Wan X, Jimenez JC, et al: Nonlinear local electrovascular coupling. I: A theoretical model. Hum Brain Mapp 27:896-914, 2006
19. Riera JJ, Jimenez JC, Wan X, et al: Nonlinear local electrovascular coupling. II: From data to neuronal masses. Hum Brain Mapp 28:335-354, 2007
20. Daunizeau J, Grova C, Marrelec G, et al: Symmetrical event-related EEG/fMRI information fusion in a variational Bayesian framework. Neuroimage 36:69-87, 2007
21. Sotero RC, Trujillo-Barreto NJ: Biophysical model for integrating neuronal activity, EEG, fMRI and metabolism. Neuroimage 39:290-309, 2008
22. Brookings T, Ortigue S, Grafton S, et al: Using ICA and realistic BOLD models to obtain joint EEG/fMRI solutions to the problem of source localization. Neuroimage 44:411-420, 2009
23. Mulert C, Lemieux L: EEG - fMRI: Physiological Basis, Technique, and Applications. Springer, 2009
24. Ullsperger M, Debener S: Simultaneous EEG and fMRI: Recording, Analysis, and Application. Oxford University Press, USA, 2010
25. Niedermeyer E, Lopes da Silva F: Electroencephalography: Basic Principles, Clinical Applications, and Related Fields. Lippincott Williams & Wilkins, 2004
26. Nunez PL: Neocortical Dynamics and Human EEG Rhythms. Oxford University Press, USA, 1995
27. Goto T, Hatanaka R, Ogawa T, et al: An evaluation of the conductivity profile in the somatosensory barrel cortex of wistar rats. J Neurophysiol 104:3388-3412, 2010
28. Oostendorp TF, Delbeke J, Stegeman DF: The conductivity of the human skull: results of in vivo and in vitro measurements. IEEE Trans Biomed Eng 47:1487-1492, 2000
29. Lai Y, van Drongelen W, Ding L, et al: Estimation of in vivo human brain-to-skull conductivity ratio from simultaneous extra- and intra-cranial electrical potential recordings. Clin Neurophysiol 116:456-465, 2005
30. Bloch F, Hansen WW, Packard M: Nuclear induction. Phys Rev 69:127-127, 1946
31. Purcell EM, Torrey HC, Pound RV: Resonance absorption by nuclear magnetic moments in a solid. Phys Rev 69:37-37, 1946
32. Ogawa S, Lee TM, Kay AR, et al: Brain magnetic resonance imaging with contrast dependent on blood oxygenation. Proc Natl Acad Sci U S A 87:9868-9872, 1990
33. Bandettini PA, Wong EC, Hinks RS, et al: Time course EPI of human brain function

during task activation. Magn Reson Med 25:390-397, 1992
34. Kwong KK, Belliveau JW, Chesler DA, et al: Dynamic magnetic resonance imaging of human brain activity during primary sensory stimulation. Proc Natl Acad Sci U S A 89:5675-5679, 1992
35. Ogawa S, Tank DW, Menon R, et al: Intrinsic signal changes accompanying sensory stimulation: functional brain mapping with magnetic resonance imaging. Proc Natl Acad Sci U S A 89:5951-5955, 1992
36. Buxton RB: Introduction to Functional Magnetic Resonance Imaging: Principles and Techniques. Cambridge University Press, 2002
37. Riera JJ, Sumiyoshi A: Brain oscillations: ideal scenery to understand the neurovascular coupling. Curr Opin Neurol 23:374-381, 2010
38. Iadecola C: Neurovascular regulation in the normal brain and in Alzheimer's disease. Nat Rev Neurosci 5:347-360, 2004
39. Zonta M, Angulo MC, Gobbo S, et al: Neuron-to-astrocyte signaling is central to the dynamic control of brain microcirculation. Nat Neurosci 6:43-50, 2003
40. Girouard H, Iadecola C: Neurovascular coupling in the normal brain and in hypertension, stroke, and Alzheimer disease. J Appl Physiol 100:328-335, 2006
41. Takano T, Tian G-F, Peng W, et al: Astrocyte-mediated control of cerebral blood flow. Nat Neurosci 9:260-267, 2006
42. Wang X, Lou N, Xu Q, et al: Astrocytic Ca2+ signaling evoked by sensory stimulation in vivo. Nat Neurosci 9:816-823, 2006
43. Iadecola C, Nedergaard M: Glial regulation of the cerebral microvasculature. Nat Neurosci 10:1369-1376, 2007
44. Logothetis NK, Pauls J, Augath M, et al: Neurophysiological investigation of the basis of the fMRI signal. Nature 412:150-157, 2001
45. Goense JBM, Logothetis NK: Neurophysiology of the BOLD fMRI signal in awake monkeys. Curr Biol 18:631-640, 2008
46. Wan X, Riera JJ, Iwata K, et al: The neural basis of the hemodynamic response nonlinearity in human primary visual cortex: Implications for neurovascular coupling mechanism. Neuroimage 32:616-625, 2006
47. Shmuel A, Augath M, Oeltermann A, et al: Negative functional MRI response correlates with decreases in neuronal activity in monkey visual area V1. Nat Neurosci 9:569-577, 2006
48. Ives JR, Warach S, Schmitt F, et al: Monitoring the patient's EEG during echo planar MRI. Electroencephalogr Clin Neurophysiol 87:417-420, 1993
49. Lemieux L, Allen PJ, Franconi F, et al: Recording of EEG during fMRI experiments: patient safety. Magn Reson Med 38:943-952, 1997
50. Lufkin R, Jordan S, Lylyck P, et al: MR imaging with topographic EEG electrodes in place. AJNR Am J Neuroradiol 9:953-954, 1988

51. Krakow K, Allen PJ, Symms MR, et al: EEG recording during fMRI experiments: image quality. Hum Brain Mapp 10:10-15, 2000
52. Allen PJ, Polizzi G, Krakow K, et al: Identification of EEG events in the MR scanner: the problem of pulse artifact and a method for its subtraction. Neuroimage 8:229-239, 1998
53. Allen PJ, Josephs O, Turner R: A method for removing imaging artifact from continuous EEG recorded during functional MRI. Neuroimage 12:230-239, 2000
54. Salek-Haddadi A, Friston KJ, Lemieux L, et al: Studying spontaneous EEG activity with fMRI. Brain Res Brain Res Rev 43:110-133, 2003
55. Ritter P, Villringer A: Simultaneous EEG-fMRI. Neurosci Biobehav Rev 30:823-838, 2006
56. Herrmann CS, Debener S: Simultaneous recording of EEG and BOLD responses: a historical perspective. Int J Psychophysiol 67:161-168, 2008
57. Laufs H, Daunizeau J, Carmichael DW, et al: Recent advances in recording electrophysiological data simultaneously with magnetic resonance imaging. Neuroimage 40:515-528, 2008
58. Christmann C, Ruf M, Braus DF, et al: Simultaneous electroencephalography and functional magnetic resonance imaging of primary and secondary somatosensory cortex in humans after electrical stimulation. Neurosci Lett 333:69-73, 2002
59. Liebenthal E, Ellingson ML, Spanaki MV, et al: Simultaneous ERP and fMRI of the auditory cortex in a passive oddball paradigm. Neuroimage 19:1395-1404, 2003
60. Comi E, Annovazzi P, Silva AM, et al: Visual evoked potentials may be recorded simultaneously with fMRI scanning: A validation study. Hum Brain Mapp 24:291-298, 2005
61. Lövblad KO, Thomas R, Jakob PM, et al: Silent functional magnetic resonance imaging demonstrates focal activation in rapid eye movement sleep. Neurology 53:2193-2195, 1999
62. Lemieux L, Salek-Haddadi A, Josephs O, et al: Event-related fMRI with simultaneous and continuous EEG: description of the method and initial case report. Neuroimage 14:780-787, 2001
63. Scarff CJ, Reynolds A, Goodyear BG, et al: Simultaneous 3-T fMRI and high-density recording of human auditory evoked potentials. Neuroimage 23:1129-1142, 2004
64. Vasios CE, Angelone LM, Purdon PL, et al: EEG/(f)MRI measurements at 7 Tesla using a new EEG cap ("InkCap"). Neuroimage 33:1082-1092, 2006
65. Busch E, Hoehn-Berlage M, Eis M, et al: Simultaneous recording of EEG, DC potential and diffusion-weighted NMR imaging during potassium induced cortical spreading depression in rats. NMR Biomed 8:59-64, 1995
66. Brinker G, Bock C, Busch E, et al: Simultaneous recording of evoked potentials and T2*-weighted MR images during somatosensory stimulation of rat. Magn Reson Med

41:469-473, 1999

67. Mirsattari SM, Ives JR, Leung LS, et al: EEG monitoring during functional MRI in animal models. Epilepsia 48 Suppl 4:37-46, 2007
68. Wan X, Iwata K, Riera JJ, et al: Artifact reduction for simultaneous EEG/fMRI recording: adaptive FIR reduction of imaging artifacts. Clin Neurophysiol 117:681-692, 2006
69. Wan X, Iwata K, Riera JJ, et al: Artifact reduction for EEG/fMRI recording: nonlinear reduction of ballistocardiogram artifacts. Clin Neurophysiol 117:668-680, 2006
70. Mégevand P, Quairiaux C, Lascano AM, et al: A mouse model for studying large-scale neuronal networks using EEG mapping techniques. Neuroimage 42:591-602, 2008
71. Baumann SB, Noll DC: A modified electrode cap for EEG recordings in MRI scanners. Clin Neurophysiol 110:2189-2193, 1999
72. Bonmassar G, Nouchine H, John RI, et al: Influence of EEG electrodes on the BOLD fMRI signal. Hum Brain Mapp 14:108-115, 2001
73. Tallgren P, Vanhatalo S, Kaila K, et al: Evaluation of commercially available electrodes and gels for recording of slow EEG potentials. Clin Neurophysiol 116:799-806, 2005
74. Mullinger K, Debener S, Coxon R, et al: Effects of simultaneous EEG recording on MRI data quality at 1.5, 3 and 7 tesla. Int J Psychophysiol 67:178-188, 2008
75. Wood AK, Klide AM, Pickup S, et al: Prolonged general anesthesia in MR studies of rats. Acad Radiol 8:1136-1140, 2001
76. Smith AJ, Blumenfeld H, Behar KL, et al: Cerebral energetics and spiking frequency: the neurophysiological basis of fMRI. Proc Natl Acad Sci U S A 99:10765-10770, 2002
77. Maandag NJG, Coman D, Sanganahalli BG, et al: Energetics of neuronal signaling and fMRI activity. Proc Natl Acad Sci U S A 104:20546-20551, 2007
78. Mandeville JB, Marota JJ, Kosofsky BE, et al: Dynamic functional imaging of relative cerebral blood volume during rat forepaw stimulation. Magn Reson Med 39:615-624, 1998
79. Sachdev RNS, Champney GC, Lee H, et al: Experimental model for functional magnetic resonance imaging of somatic sensory cortex in the unanesthetized rat. Neuroimage 19:742-750, 2003
80. Sicard KM, Duong TQ: Effects of hypoxia, hyperoxia, and hypercapnia on baseline and stimulus-evoked BOLD, CBF, and CMRO2 in spontaneously breathing animals. Neuroimage 25:850-858, 2005
81. Wibral M, Muckli L, Melnikovic K, et al: Time-dependent effects of hyperoxia on the BOLD fMRI signal in primate visual cortex and LGN. Neuroimage 35:1044-1063, 2007
82. Zappe AC, Uludag K, Logothetis NK: Direct measurement of oxygen extraction with fMRI using 6% CO2 inhalation. Magn Reson Imaging 26:961-967, 2008
83. Mirsattari SM, Bihari F, Leung LS, et al: Physiological monitoring of small animals during magnetic resonance imaging. J Neurosci Methods 144:207-213, 2005

84. Ureshi M, Kershaw J, Kanno I: Nonlinear correlation between field potential and local cerebral blood flow in rat somatosensory cortex evoked by changing the stimulus current. Neurosci Res 51:139-145, 2005
85. Zheng Y, Pan Y, Harris S, et al: A dynamic model of neurovascular coupling: implications for blood vessel dilation and constriction. Neuroimage 52:1135-1147, 2010
86. Fu R, Brey WW, Shetty K, et al: Ultra-wide bore 900 MHz high-resolution NMR at the National High Magnetic Field Laboratory. J Magn Reson 177:1-8, 2005
87. Schepkin VD, Brey WW, Gor'kov PL, et al: Initial in vivo rodent sodium and proton MR imaging at 21.1 T. Magn Reson Imaging 28:400-407, 2010
88. Hyder F, Chase JR, Behar KL, et al: Increased tricarboxylic acid cycle flux in rat brain during forepaw stimulation detected with 1H[13C]NMR. Proc Natl Acad Sci U S A 93:7612-7617, 1996
89. Zhu X-H, Zhang Y, Tian R-X, et al: Development of (17)O NMR approach for fast imaging of cerebral metabolic rate of oxygen in rat brain at high field. Proc Natl Acad Sci U S A 99:13194-13199, 2002
90. Tailor DR, Roy A, Regatte RR, et al: Indirect 17(O)-magnetic resonance imaging of cerebral blood flow in the rat. Magn Reson Med 49:479-487, 2003
91. Hyder F, Behar KL, Martin MA, et al: Dynamic magnetic resonance imaging of the rat brain during forepaw stimulation. J Cereb Blood Flow Metab 14:649-655, 1994
92. Meyer CR, Moffat BA, Kuszpit KK, et al: A methodology for registration of a histological slide and in vivo MRI volume based on optimizing mutual information. Mol Imaging 5:16-23, 2006
93. Leergaard TB, White NS, de Crespigny A, et al: Quantitative histological validation of diffusion MRI fiber orientation distributions in the rat brain. PloS One 5:e8595-e8595,
94. Steward CA, Marsden CA, Prior MJW, et al: Methodological considerations in rat brain BOLD contrast pharmacological MRI. Psychopharmacology 180:687-704, 2005
95. Blumenfeld H: Functional MRI studies of animal models in epilepsy. Epilepsia 48 Suppl 4:18-26, 2007
96. Logothetis NK, Wandell BA: Interpreting the BOLD signal. Annu Rev Physiol 66:735-769, 2004
97. Cauli B, Hamel E: Revisiting the role of neurons in neurovascular coupling. Front Neuroenergetics 2:9-9, 2010
98. Lu H, Zuo Y, Gu H, et al: Synchronized delta oscillations correlate with the resting-state functional MRI signal. Proc Natl Acad Sci U S A 104:18265-18269, 2007
99. Endo T, Spenger C, Tominaga T, et al: Cortical sensory map rearrangement after spinal cord injury: fMRI responses linked to Nogo signalling. Brain 130:2951-2961, 2007
100. Gyngell ML, Bock C, Schmitz B, et al: Variation of functional MRI signal in response to frequency of somatosensory stimulation in alpha-chloralose anesthetized rats. Magn Reson Med 36:13-15, 1996

101. Silva AC, Kim SG: Pseudo-continuous arterial spin labeling technique for measuring CBF dynamics with high temporal resolution. Magn Reson Med 42:425-429, 1999
102. Ogawa S, Lee TM, Stepnoski R, et al: An approach to probe some neural systems interaction by functional MRI at neural time scale down to milliseconds. Proc Natl Acad Sci U S A 97:11026-11031, 2000
103. Spenger C, Josephson A, Klason T, et al: Functional MRI at 4.7 tesla of the rat brain during electric stimulation of forepaw, hindpaw, or tail in single- and multislice experiments. Exp Neurol 166:246-253, 2000
104. Friedman L, Glover GH: Report on a multicenter fMRI quality assurance protocol. J Magn Reson Imaging 23:827-839, 2006
105. Schneiders NJ: Solutions of two paramagnetic ions for use in nuclear magnetic resonance phantoms. Med Phys 15:12-16, 1988
106. Angelone LM, Vasios CE, Wiggins G, et al: On the effect of resistive EEG electrodes and leads during 7 T MRI: simulation and temperature measurement studies. Magn Reson Imaging 24:801-812, 2006
107. Sanganahalli BG, Bailey CJ, Herman P, et al: Tactile and non-tactile sensory paradigms for fMRI and neurophysiologic studies in rodents. Methods Mol Biol 489:213-242, 2009
108. Schweinhardt P, Fransson P, Olson L, et al: A template for spatial normalisation of MR images of the rat brain. J Neurosci Methods 129:105-113, 2003
109. Paxinos G, Watson C: The Rat Brain in Stereotaxic Coordinates, Sixth Edition. Academic Press, 2007
110. Rohr K, Stiehl HS, Sprengel R, et al: Landmark-based elastic registration using approximating thin-plate splines. IEEE Trans Med Imaging 20:526-534, 2001
111. Uberti MG, Boska MD, Liu Y: A semi-automatic image segmentation method for extraction of brain volume from in vivo mouse head magnetic resonance imaging using Constraint Level Sets. J Neurosci Methods 179:338-344, 2009
112. Haacke EM, Brown RW, Thompson MR, et al: Magnetic Resonance Imaging: Physical Principles and Sequence Design. Wiley-Liss, 1999
113. Wood AW, Hamblin DL, Croft RJ: The use of a 'phantom scalp' to assess the possible direct pickup of mobile phone handset emissions by electroencephalogram electrode leads. Med Biol Eng Comput 41:470-472, 2003
114. Seehafer JU, Kalthoff D, Farr TD, et al: No increase of the blood oxygenation level-dependent functional magnetic resonance imaging signal with higher field strength: implications for brain activation studies. J Neurosci 30:5234-5241, 2010
115. Jarque CM, Bera AK: A test for normality of observations and regression residuals. Int Stat Rev 55:163-172, 1987
116. Lazeyras F, Zimine I, Blanke O, et al: Functional MRI with simultaneous EEG recording: feasibility and application to motor and visual activation. J Magn Reson

Imaging 13:943-948, 2001
117. Meriläinen V: Magnetic resonance imaging with simultaneous electroencephalography recording: safety issues. Master Thesis (Helsinki University of Technology) 2002
118. IEC: Medical electrical equipment—particular requirements for the safety of magnetic resonance equipment for medical diagnosis. IEC 60601-2-33, 2002
119. Angelone LM, Potthast A, Segonne F, et al: Metallic electrodes and leads in simultaneous EEG-MRI: specific absorption rate (SAR) simulation studies. Bioelectromagnetics 25:285-295, 2004
120. Paxinos G, Watson C: The Rat Brain in Stereotaxic Coordinates, First Edition. Academic Press, 1982
121. Hoult DI, Lauterbur PC: The sensitivity of the zeugmatographic experiment involving human samples. J Magn Reson 34:425-433, 1979
122. Stefanovic B, Schwindt W, Hoehn M, et al: Functional uncoupling of hemodynamic from neuronal response by inhibition of neuronal nitric oxide synthase. J Cereb Blood Flow Metab 27:741-754, 2007
123. Huttunen JK, Gröhn O, Penttonen M: Coupling between simultaneously recorded BOLD response and neuronal activity in the rat somatosensory cortex. Neuroimage 39:775-785, 2008
124. Debener S, Mullinger KJ, Niazy RK, et al: Properties of the ballistocardiogram artefact as revealed by EEG recordings at 1.5, 3 and 7 T static magnetic field strength. Int J Psychophysiol 67:189-199, 2008
125. Sijbers J, Van Audekerke J, Verhoye M, et al: Reduction of ECG and gradient related artifacts in simultaneously recorded human EEG/MRI data. Magn Reson Imaging 18:881-886, 2000
126. Franceschini MA, Radhakrishnan H, Thakur K, et al: The effect of different anesthetics on neurovascular coupling. Neuroimage 51:1367-1377, 2010
127. Ferezou I, Haiss F, Gentet LJ, et al: Spatiotemporal dynamics of cortical sensorimotor integration in behaving mice. Neuron 56:907-923, 2007
128. de Celis Alonso B, Lowe AS, Dear JP, et al: Sensory inputs from whisking movements modify cortical whisker maps visualized with functional magnetic resonance imaging. Cereb Cortex 18:1314-1325, 2008
129. Lu H, Scholl CA, Zuo Y, et al: Registering and analyzing rat fMRI data in the stereotaxic framework by exploiting intrinsic anatomical features. Magn Reson Imaging 28:146-152, 2010
130. Dale AM, Liu AK, Fischl BR, et al: Dynamic statistical parametric mapping: combining fMRI and MEG for high-resolution imaging of cortical activity. Neuron 26:55-67, 2000
131. Vitacco D, Brandeis D, Pascual-Marqui R, et al: Correspondence of event-related potential tomography and functional magnetic resonance imaging during language processing. Hum Brain Mapp 17:4-12, 2002

132. Miwakeichi F, Martínez-Montes E, Valdés-Sosa PA, et al: Decomposing EEG data into space-time-frequency components using Parallel Factor Analysis. Neuroimage 22:1035-1045, 2004
133. Riera JJ, Sumiyoshi A, Kawashima R: Japanese patent application. JP2010-098320 filed April 21, 2010
134. Mantini D, Perrucci MG, Del Gratta C, et al: Electrophysiological signatures of resting state networks in the human brain. Proc Natl Acad Sci U S A 104:13170-13175, 2007
135. Schwarz AJ, Danckaert A, Reese T, et al: A stereotaxic MRI template set for the rat brain with tissue class distribution maps and co-registered anatomical atlas: application to pharmacological MRI. Neuroimage 32:538-550, 2006
136. Pawela CP, Biswal BB, Cho YR, et al: Resting-state functional connectivity of the rat brain. Magn Reson Med 59:1021-1029, 2008
137. Bifone A, Gozzi A, Schwarz AJ: Functional connectivity in the rat brain: a complex network approach. Magn Reson Imaging 28:1200-1209, 2010
138. Magnuson M, Majeed W, Keilholz SD: Functional connectivity in blood oxygenation level-dependent and cerebral blood volume-weighted resting state functional magnetic resonance imaging in the rat brain. J Magn Reson Imaging 32:584-592, 2010
139. Sanabria-Diaz G, Melie-García L, Iturria-Medina Y, et al: Surface area and cortical thickness descriptors reveal different attributes of the structural human brain networks. Neuroimage 50:1497-1510, 2010
140. Devor A, Hillman EMC, Tian P, et al: Stimulus-induced changes in blood flow and 2-deoxyglucose uptake dissociate in ipsilateral somatosensory cortex. J Neurosci 28:14347-14357, 2008
141. Austin VC, Blamire AM, Allers KA, et al: Confounding effects of anesthesia on functional activation in rodent brain: a study of halothane and alpha-chloralose anesthesia. Neuroimage 24:92-100, 2005
142. Boas DA, Jones SR, Devor A, et al: A vascular anatomical network model of the spatio-temporal response to brain activation. Neuroimage 40:1116-1129, 2008
143. Yücel MA, Devor A, Akin A, et al: The Possible Role of CO(2) in Producing A Post-Stimulus CBF and BOLD Undershoot. Front Neuroenergetics 1:7-7, 2009
144. Hirase H: A multi-photon window onto neuronal-glial-vascular communication. Trends Neurosci 28:217-219, 2005
145. Bakalova R, Matsuura T, Kanno I: The cyclooxygenase inhibitors indomethacin and Rofecoxib reduce regional cerebral blood flow evoked by somatosensory stimulation in rats. Exp Biol Med (Maywood) 227:465-473, 2002
146. Niwa K, Haensel C, Ross ME, et al: Cyclooxygenase-1 participates in selected vasodilator responses of the cerebral circulation. Circ Res 88:600-608, 2001
147. Buchsbaum MS, Kessler R, King A, et al: Simultaneous cerebral glucography with positron emission tomography and topographic electroencephalography. Prog Brain Res

62:263-269, 1984
148. Hoshi Y, Mizukami S, Tamura M: Dynamic features of hemodynamic and metabolic changes in the human brain during all-night sleep as revealed by near-infrared spectroscopy. Brain Res 652:257-262, 1994
149. Salustri C, Chapman RM: A simple method for 3-dimensional localization of epileptic activity recorded by simultaneous EEG and MEG. Electroencephalogr Clin Neurophysiol 73:473-478, 1989
150. Mackert B-M, Wübbeler G, Leistner S, et al: Neurovascular coupling analyzed non-invasively in the human brain. Neuroreport 15:63-66, 2004
151. Zotev VS, Matlashov AN, Volegov PL, et al: Microtesla MRI of the human brain combined with MEG. J Magn Reson 194:115-120, 2008
152. Villringer K, Minoshima S, Hock C, et al: Assessment of local brain activation. A simultaneous PET and near-infrared spectroscopy study. Adv Exp Med Biol 413:149-153, 1997
153. Kleinschmidt A, Obrig H, Requardt M, et al: Simultaneous recording of cerebral blood oxygenation changes during human brain activation by magnetic resonance imaging and near-infrared spectroscopy. J Cereb Blood Flow Metab 16:817-826, 1996
154. Judenhofer MS, Wehrl HF, Newport DF, et al: Simultaneous PET-MRI: a new approach for functional and morphological imaging. Nat Med 14:459-465, 2008
155. Wansapura JP, Holland SK, Dunn RS, et al: NMR relaxation times in the human brain at 3.0 tesla. J Magn Reson Imaging 9:531-538, 1999
156. Opdam HI, Federico P, Jackson GD, et al: A sheep model for the study of focal epilepsy with concurrent intracranial EEG and functional MRI. Epilepsia 43:779-787, 2002
157. Van Camp N, D'Hooge R, Verhoye M, et al: Simultaneous electroencephalographic recording and functional magnetic resonance imaging during pentylenetetrazol-induced seizures in rat. Neuroimage 19:627-636, 2003
158. Nersesyan H, Hyder F, Rothman DL, et al: Dynamic fMRI and EEG recordings during spike-wave seizures and generalized tonic-clonic seizures in WAG/Rij rats. J Cereb Blood Flow Metab 24:589-599, 2004
159. Mäkiranta M, Ruohonen J, Suominen K, et al: BOLD signal increase preceeds EEG spike activity--a dynamic penicillin induced focal epilepsy in deep anesthesia. Neuroimage 27:715-724, 2005
160. Schmid MC, Oeltermann A, Juchem C, et al: Simultaneous EEG and fMRI in the macaque monkey at 4.7 Tesla. Magn Reson Imaging 24:335-342, 2006
161. David O, Guillemain I, Saillet S, et al: Identifying neural drivers with functional MRI: an electrophysiological validation. PLoS Biol 6:2683-2697, 2008
162. DeSalvo MN, Schridde U, Mishra AM, et al: Focal BOLD fMRI changes in bicuculline-induced tonic-clonic seizures in the rat. Neuroimage 50:902-909, 2010
163. Tenney JR, Duong TQ, King JA, et al: Corticothalamic modulation during absence

seizures in rats: a functional MRI assessment. Epilepsia 44:1133-1140, 2003
164. Englot DJ, Mishra AM, Mansuripur PK, et al: Remote effects of focal hippocampal seizures on the rat neocortex. J Neurosci 28:9066-9081, 2008
165. Wadghiri YZ, Sigurdsson EM, Sadowski M, et al: Detection of Alzheimer's amyloid in transgenic mice using magnetic resonance microimaging. Magn Reson Med 50:293-302, 2003
166. Wu EX, Tang H, Asai T, et al: Regional cerebral blood volume reduction in transgenic mutant APP (V717F, K670N/M671L) mice. Neurosci Lett 365:223-227, 2004
167. Higuchi M, Iwata N, Matsuba Y, et al: 19F and 1H MRI detection of amyloid beta plaques in vivo. Nat Neurosci 8:527-533, 2005
168. Lau JC, Lerch JP, Sled JG, et al: Longitudinal neuroanatomical changes determined by deformation-based morphometry in a mouse model of Alzheimer's disease. Neuroimage 42:19-27, 2008
169. Pelled G, Bergman H, Ben-Hur T, et al: Reduced basal activity and increased functional homogeneity in sensorimotor and striatum of a Parkinson's disease rat model: a functional MRI study. Eur J Neurosci 21:2227-2232, 2005
170. Van Camp N, Blockx I, Verhoye M, et al: Diffusion tensor imaging in a rat model of Parkinson's disease after lesioning of the nigrostriatal tract. NMR Biomed 22:697-706, 2009
171. Hou Z, Lei H, Hong S, et al: Functional changes in the frontal cortex in Parkinson's disease using a rat model. J Clin Neurosci 17:628-633, 2010
172. Beckmann N, Stirnimann R, Bochelen D: High-resolution magnetic resonance angiography of the mouse brain: application to murine focal cerebral ischemia models. J Magn Reson 140:442-450, 1999
173. Li F, Liu KF, Silva MD, et al: Transient and permanent resolution of ischemic lesions on diffusion-weighted imaging after brief periods of focal ischemia in rats : correlation with histopathology. Stroke 31:946-954, 2000
174. Aoki I, Ebisu T, Tanaka C, et al: Detection of the anoxic depolarization of focal ischemia using manganese-enhanced MRI. Magn Reson Med 50:7-12, 2003
175. Ramu J, Bockhorst KH, Mogatadakala KV, et al: Functional magnetic resonance imaging in rodents: Methodology and application to spinal cord injury. J Neurosci Res 84:1235-1244, 2006
176. Takagi T, Nakamura M, Yamada M, et al: Visualization of peripheral nerve degeneration and regeneration: monitoring with diffusion tensor tractography. Neuroimage 44:884-892, 2009
177. Ghosh A, Haiss F, Sydekum E, et al: Rewiring of hindlimb corticospinal neurons after spinal cord injury. Nat Neurosci 13:97-104, 2010
178. Huang W, Heffernan ME, Li Z, et al: Fear induced neuronal alterations in a genetic model of depression: an fMRI study on awake animals. Neurosci Lett 489:74-78, 2011

179. Heindl-Erdmann C, Axmann R, Kreitz S, et al: Combining functional magnetic resonance imaging with mouse genomics: new options in pain research. Neuroreport 21:29-33, 2010

## 8.2 Publication list

Scientific peer-reviewed journal *(Impact factor in 2009):*

[1] Pedro A. Valdés-Hernández*, **Akira Sumiyoshi***, Hiroi Nonaka, Risa Haga, Eubert Aubert-Vásquez, Yasser Iturria-Medina, Jorge J. Riera, Ryuta Kawashima (*equal contribution). An MRI rat template set in the Paxinos and Watson space: applications in fMRI, morphometry and anatomical connectivity. (*in revision*)

[2] **Akira Sumiyoshi**, Jorge J. Riera, Takeshi Ogawa, Ryuta Kawashima. A mini-cap for simultaneous EEG and fMRI recording in rodents. NeuroImage, 2011; 54(3):1951-1965. (*5.739*)

[3] Takakuni Goto, Rieko Hatanaka, Takeshi Ogawa, **Akira Sumiyoshi**, Jorge J. Riera, Ryuta Kawashima. An evaluation of the conductivity profile in the somatosensory barrel cortex of Wistar rats. Journal of Neurophysiology, 2010; 104(6): 3388-3412. (*3.483*)

[4] Jorge J. Riera, **Akira Sumiyoshi**. Brain oscillations: ideal scenery to understand the neurovascular coupling. Current Opinion in Neurology, 2010; 23(4):374-381. (*5.430*)

[5] Jorge J. Riera, Takeshi Ogawa, Rieko Hatanaka, Takakuni Goto, **Akira Sumiyoshi**, Herve E. Kadji, Sakura Nakauchi, Ryuta Kawashima. Concurrent observations of astrocytic Ca2+ activity and multi-site extracellular potentials from an intact cerebral cortex. Journal of Biophotonics, 2010; 3(3), 147-160. (*1.558*)

Patent:

[1] Jorge J. Riera, **Akira Sumiyoshi**, Ryuta Kawashima. Japanese patent application, JP2010-098320 (filed April 21, 2010).

Conference presentation:

[1] **Akira Sumiyoshi**, Takeshi Ogawa, Ryuta Kawashima, Jorge J. Riera. Combining EEG and fMRI data from a Wistar rat: a new tool for comparative neuroimaging. *Joint Annual Meeting ISMRM-ESMRMB 2010*, Stockholm, Sweden, May, 2010 (E-poster)

[2] **Akira Sumiyoshi**, Takeshi Ogawa, Ryuta Kawashima, Jorge J. Riera. Simultaneous EEG and fMRI recording in rodents, *14th Oxygen Dynamics Society*, Tokyo, Japan, Sep 2010 (poster)

[3] **Akira Sumiyoshi**, Hideaki Suzuki, Hiroaki Shimokawa, Ryuta Kawashima, Jorge J. Riera. Simultaneous EEG and fMRI recording in rodents, 東北大学医学系研究科主催第４回リトリート, Sendai, Japan, Jan 2011 (poster)

**Young Investigator Poster Award**

# SECTION 9 LIST OF ABBREVIATIONS AND SYMBOLS

| | |
|---|---|
| 2D | two dimensional |
| 3D | three dimensional |
| 6-OHDA | 6-hydroxydopamine |
| APP | amyloid precursor protein |
| ATPS | approximate thin plate splines |
| $B_0$ | static magnetic field |
| $B_1$ | external magnetic field |
| BOLD | blood oxygen level dependent |
| CBF | cerebral blood flow |
| CBV | cerebral blood volume |
| COX | cyclo-oxygenase |
| CYP | cytochrome P450 |
| DREAM | downstream regulatory element antagonistic modulator |
| DTI | diffusion tensor imaging |
| ECG | Electrocardiogram |
| EEG | Electroencephalogram |
| EPI | echo planar imaging |
| EPSP | excitatory postsynaptic potential |
| ERP | event-related potential |
| fMRI | functional magnetic resonance imaging |
| FOV | field of view |
| FWE | family-wise error |
| GAERS | genetic absence epilepsy rats from Strasbourg |
| GE | gradient echo |

| | |
|---|---|
| IPSP | inhibitory postsynaptic potential |
| LORETA | low resolution brain electromagnetic tomography |
| MCAO | middle cerebral artery occlusion |
| MEG | Magnetoencephalography |
| MEMRI | manganese enhanced magnetic resonance imaging |
| MGE | multiple gradient echo |
| MRI | magnetic resonance imaging |
| MRS | magnetic resonance spectroscopy |
| NIRS | near infrared optical spectroscopy |
| NMR | nuclear magnetic resonance |
| NOS | nitric oxide synthase |
| P&W | Paxinos & Watson |
| PC | principle component |
| PCA | principle component analysis |
| PET | positron emission tomography |
| phMRI | pharmacological MRI |
| PGE2 | prostaglandin E2 |
| PS1 | presenilin-1 |
| RARE | rapid acquisition with relaxation enhancement |
| RDC | radius of decorrelation |
| RF | radio frequency |
| ROI | region of interest |
| S1 | primary somatosensory are |
| SAR | specific absorption rate |
| SBW | spectral band width |

| | |
|---|---|
| SD | standard deviation |
| SE | spin echo |
| SI | signal intensity |
| SNR | signal to noise ration |
| SPM | statistical parametric mapping |
| SPECT | single photon emission computed tomography |
| Std | standard deviation |
| T | tesla |
| T1 | spin-lattice relaxation |
| T2 | spin-spin relaxation |
| TE | echo time |
| TEeff | effective echo time |
| TR | repetition time |
| VSM | vascular smooth muscle |

# SECTION 10 LIST OF FIGURES

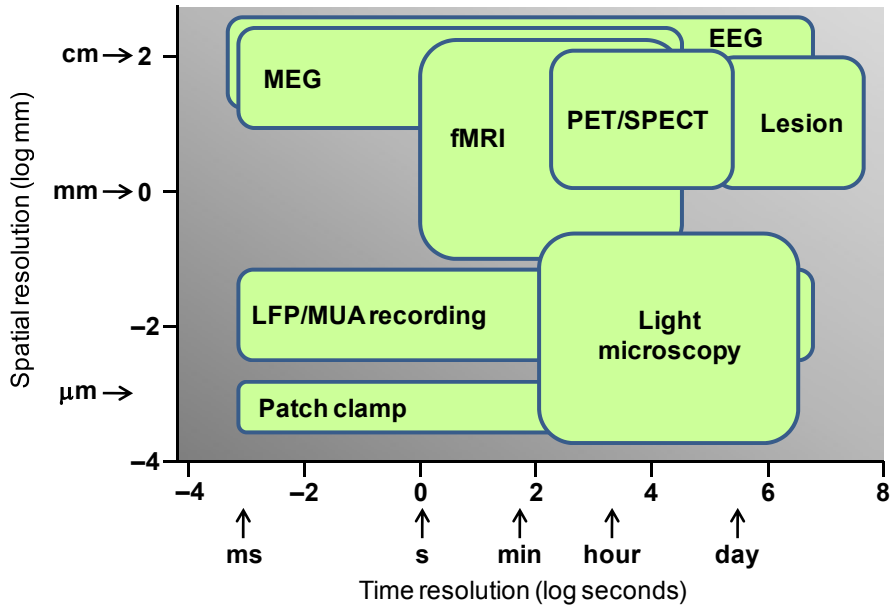


**Figure 1.1.** Comparison of spatio-temporal resolution of current methods in neuroscience.

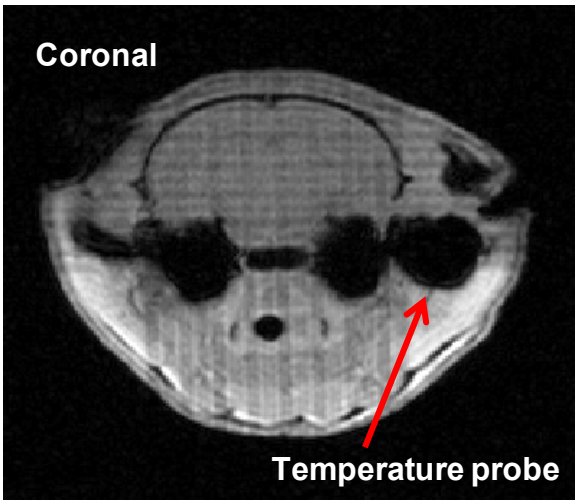


**Figure 3.1.** The position of the temperature probe in the rat's ear (red allow) is shown on a T1-weighted pilot image.

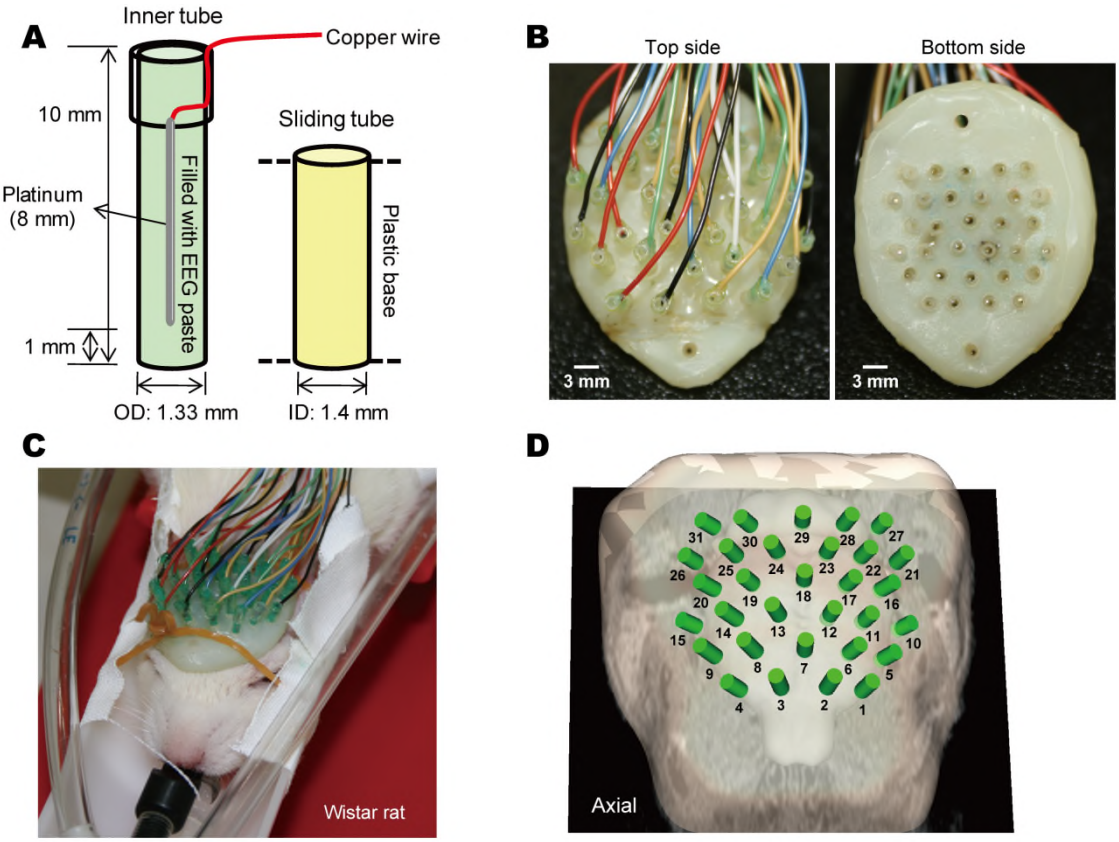


**Figure 3.2.** The MRI-compatible EEG mini-cap. (A) A schematic diagram of each electrode. The inner tube (left) contains the platinum wire (0.3 mm in diameter and 0.8 mm in length) and conductive EEG paste. The external sliding tube (right) is fixed on the plastic basement of EEG mini-cap. (B) The photograph of EEG mini-cap taken from the top side (left) and bottom side (right). (C) The photograph of EEG mini-cap placed on a Wistar rat. Each electrode is spatially arrayed with an inter-electrode distance of 3 mm to cover the whole rat head. (D) The 3D rendering of the electrodes (green cylinders) and the rat scalp and brain surfaces reconstructed from T1-weighted anatomical reference.

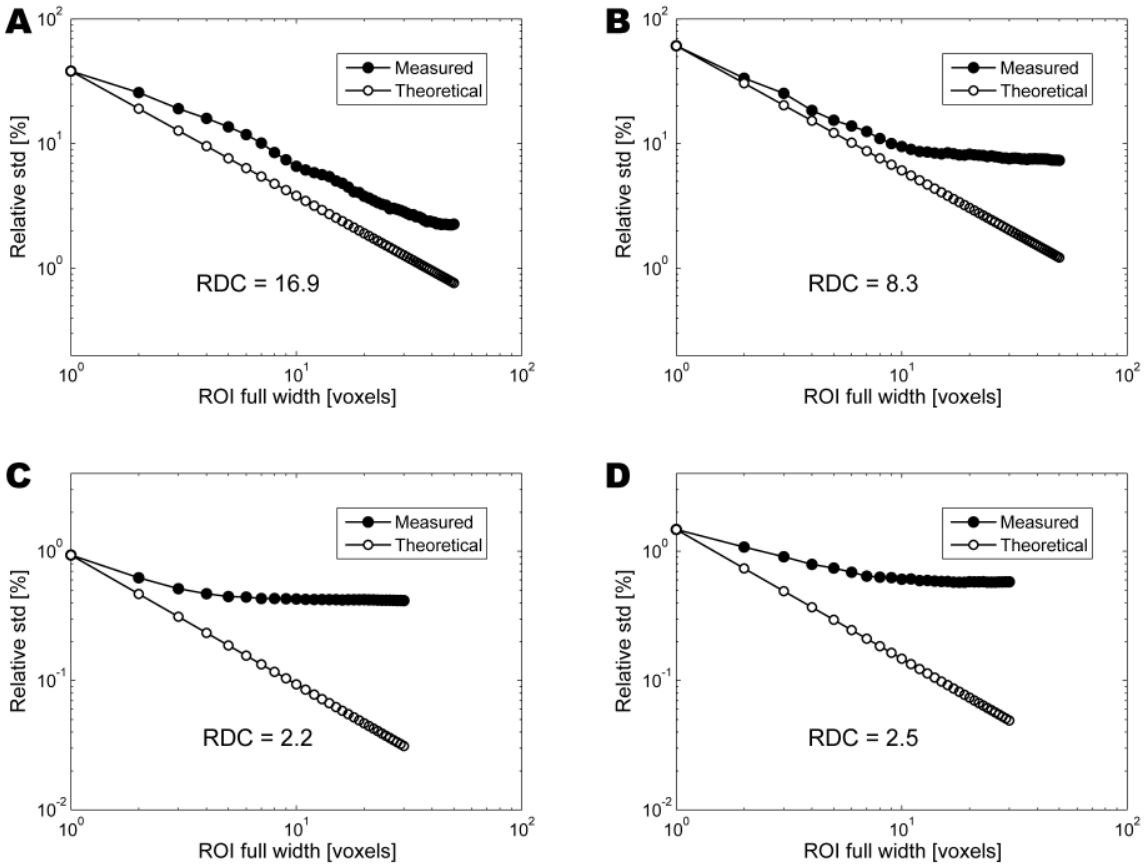


**Figure 4.1.** The Weisskoff test in the phantom. (A) and (B) panels are for the condition of transmitter-off (i.e. there is no RF excitation pulse). (C) and (D) panels are for the condition of transmitter-on (i.e. MRI phantom signal is expected). (A) and (C) panels are in the absence of EEG mini-cap. (B) and (D) panels are in the presence of EEG mini-cap. RDC: radius of decorrelation

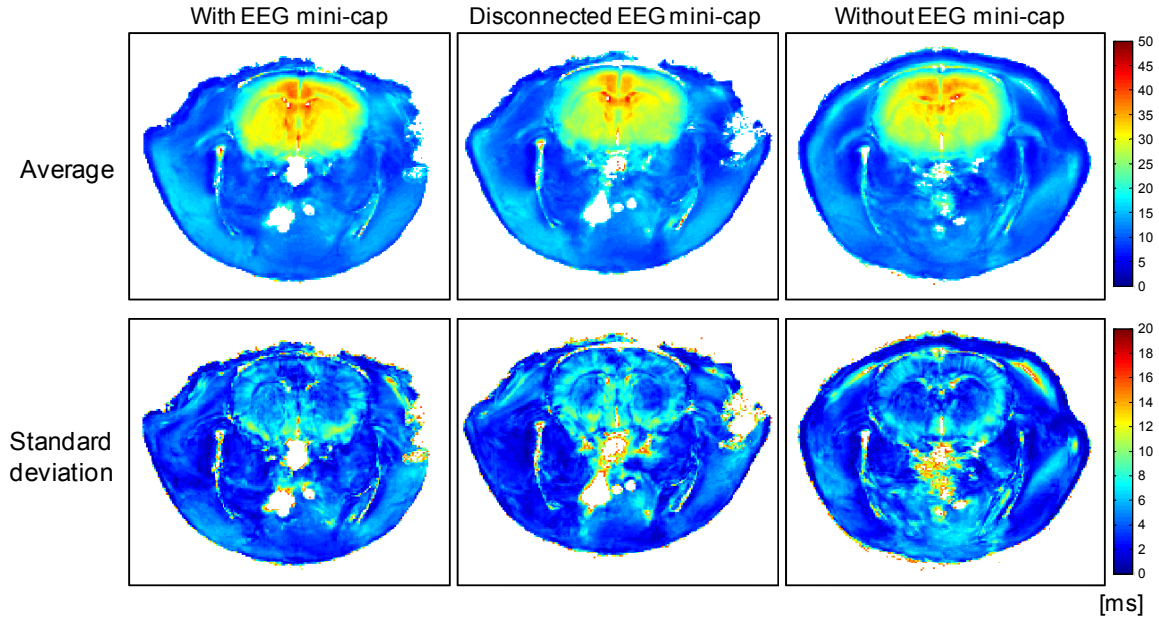


**Figure 4.2.** The T2* mapping of the rat brain ($n$ = 6). The mean (upper) and standard deviation (lower) of the T2* mapping: (left) With EEG mini-cap, (middle) Disconnected EEG mini-cap, (right) Without EEG mini-cap.

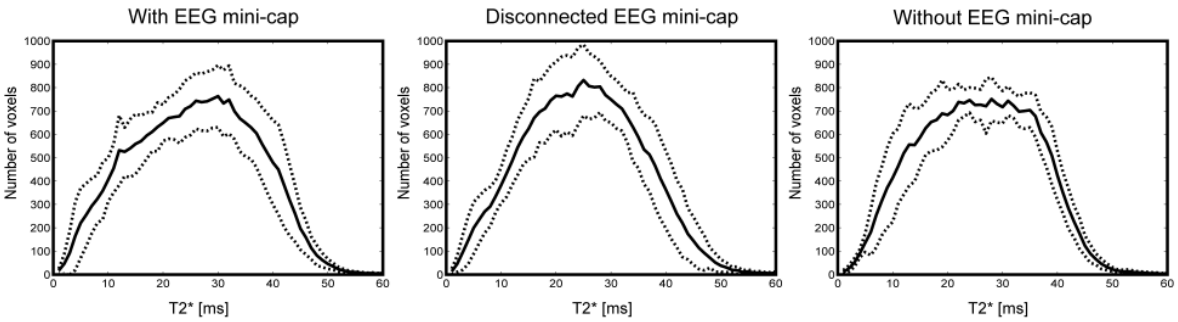


**Figure 4.3.** The histogram of T2* mapping observed in the rat brain. The solid line corresponds to the mean, while dashed lines were for the standard deviation: (left) With EEG mini-cap, (middle) Disconnected EEG mini-cap, (right) Without EEG mini-cap.

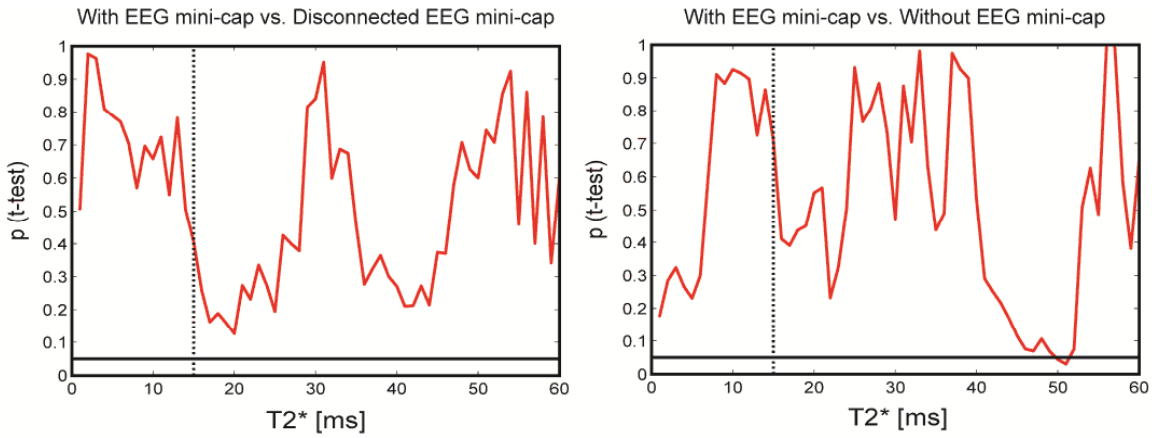


**Figure 4.4.** The result of two-sample T-test. The black solid line shows p = 0.05. The dashed line shows T2* = 15 ms, which corresponds to TE in the GE-EPI sequence used in this study: (left) The p-value of two sample T-test between With EEG mini-cap and Disconnected EEG mini-cap conditions, (right) The p-value of two sample T-test between With EEG mini-cap and Without EEG mini-cap conditions.

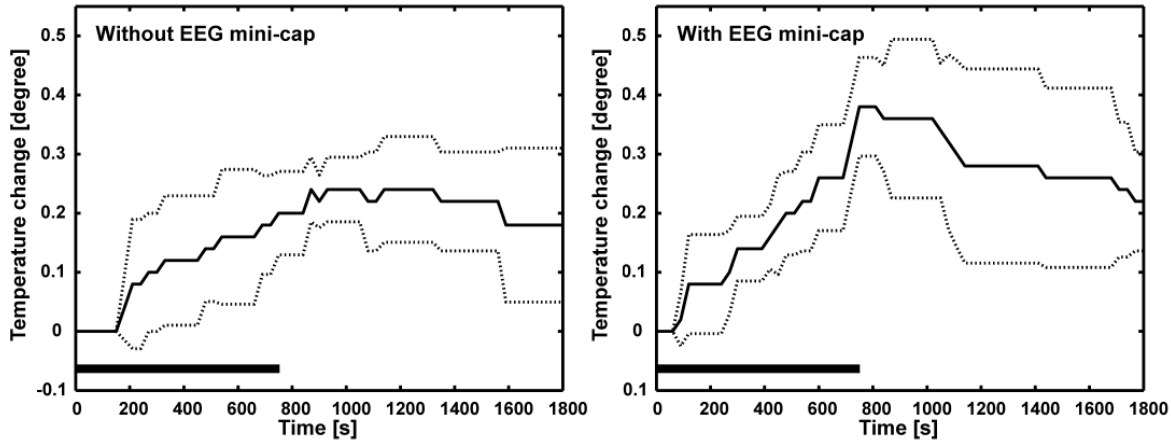


**Figure 4.5.** The temperature monitoring during GE-EPI sequences ($n$ = 5). The time-course of the temperature changes: (left) Without EEG mini-cap, (right) With connected EEG mini-cap. Note that the black horizontal bar shows the period of the applied GE-EPI sequences.

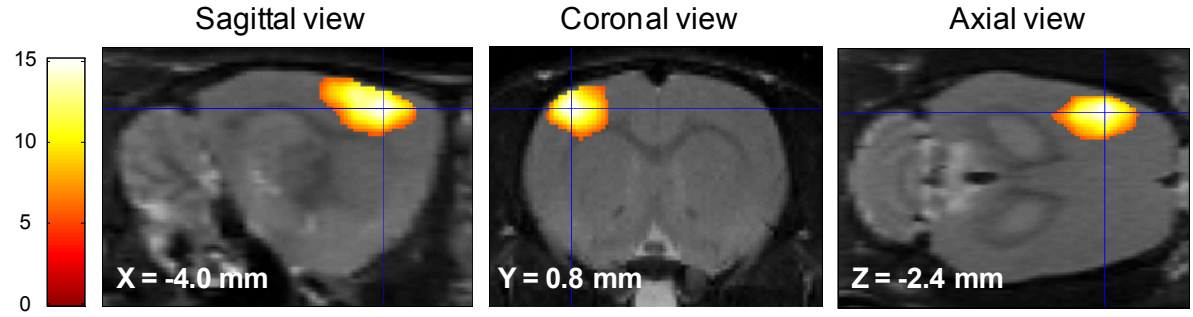


**Figure 4.6.** The SPM T-test score ($p < 0.05$) is co-registered on the rat atlas template. Note that the atlas coordinate positions are shown in mm scale: (left) sagittal view (middle), coronal view (right), axial view.

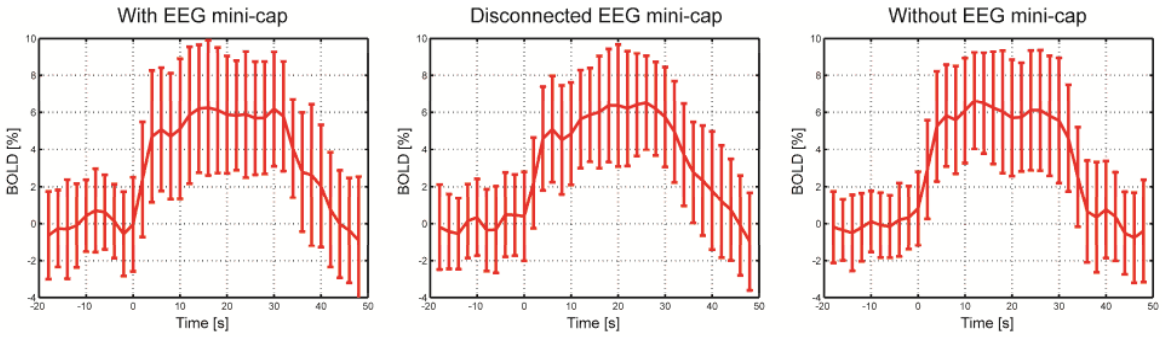


**Figure 4.7.** The fMRI signal with EEG mini-cap under the forepaw stimulation paradigm (*n* = 5). The averaged fMRI signal time course with standard deviation: (left) With EEG mini-cap, (middle) Disconnected EEG mini-cap, (right) Without EEG mini-cap.

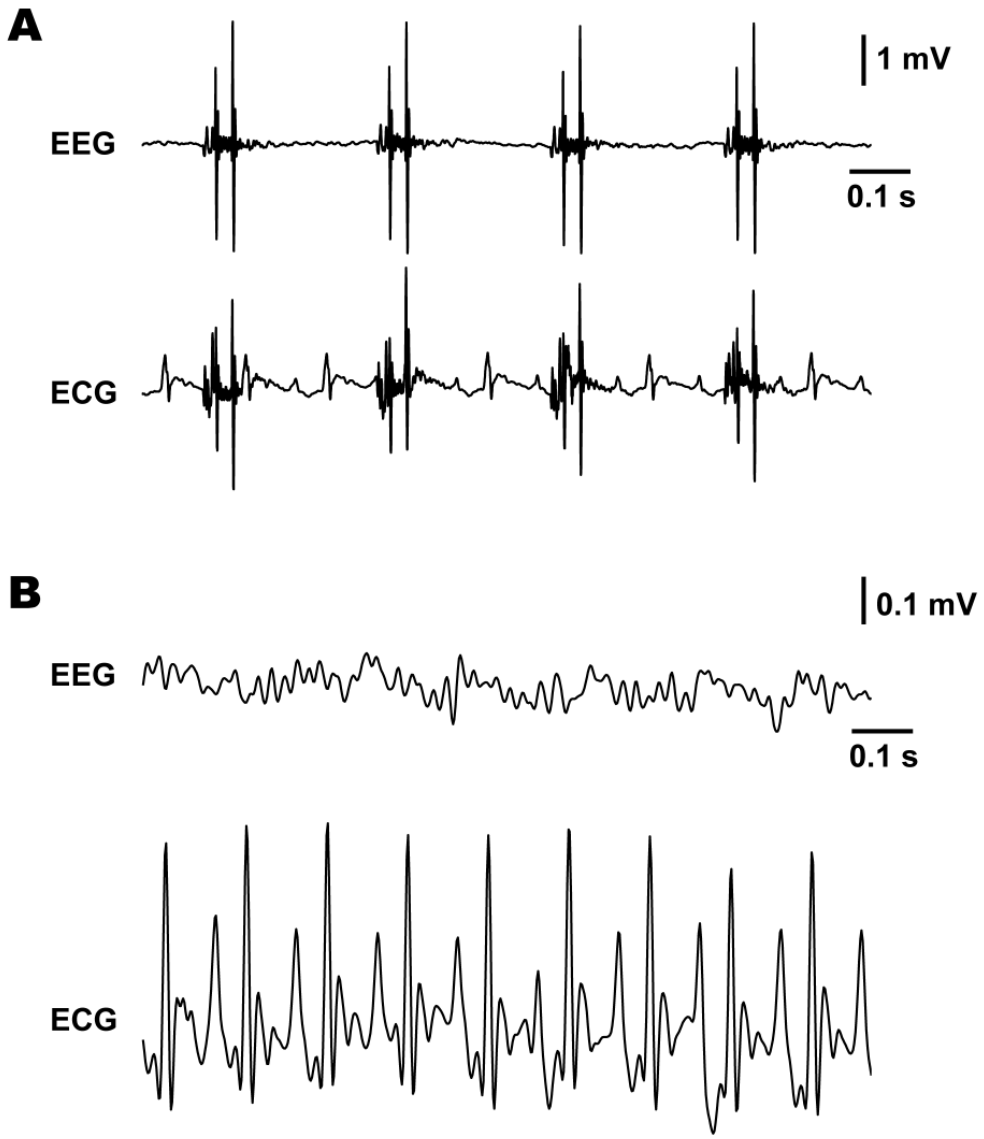
A
1 mV
EEG
0.1 s
ECG
B
0.1 mV
EEG
0.1 s
ECG
C
3000
[μV]
2000
1000
0
-1000
-2000
-3000
0
0.02
0.04
0.06
0.08
0.1
0.12
[s]
200
150
100
50
0
-50
-100
-150
-200
0.025
0.03
0.035
0.04
0.045
0.05
[s]

**Figure 4.8.** (A) One channel EEG and ECG raw data obtained from a single rat, which illustrates the presence of scanning artifacts with peak-to-peak amplitude of about 1.5–2.0 mV. (7 T MRI scanner, TR = 2000 ms and TE = 15 ms). (B) The EEG and ECG signals after removing the scanning artifacts. There is no artifact in the EEG signal correlated to the ECG signal; hence, the ballisto-cardiogram artifact can be neglected in the rodent concurrent EEG–fMRI recording. (C) The template of scanning artifact recorded at a sampling rate of 5 kHz and using a 250 Hz hardware low-pass filter.

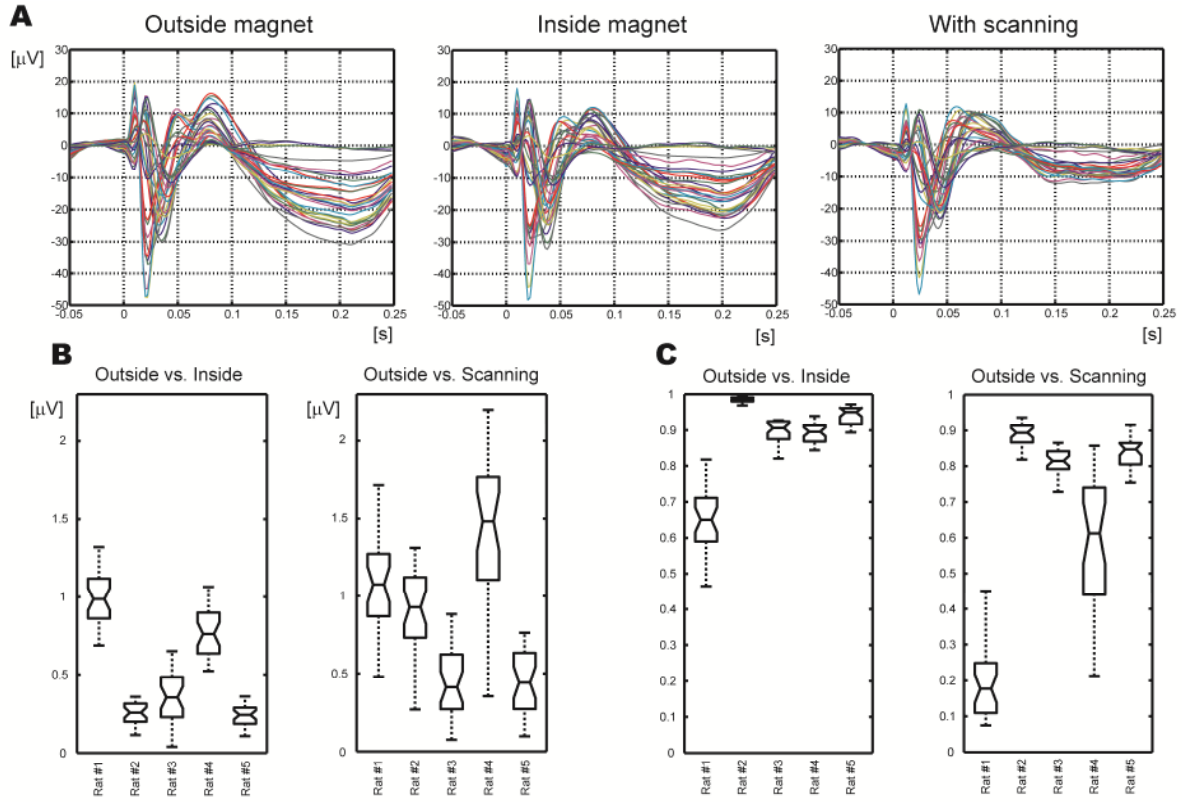


**Figure 4.9.** (A) The grant average of event-related potentials (all electrodes) for a single rat undergoing a forepaw electrical stimulation paradigm: (top) Outside MRI scanner, (middle) Inside MRI scanner, (bottom) With fMRI scanning. Note that the scanning artifacts were corrected. (B) The Euclidean distance computed for event-related potentials for pair situations: (left) between outside MRI scanner and inside MRI scanner, (right) between outside MRI scanner and with fMRI scanning. Note that the Euclidean distances are normalized by the total time points. (C) Pearson's correlation coefficients computed for event-related potentials for pair situations: (left) between outside MRI scanner and inside MRI scanner conditions, (right) between outside MRI scanner and with fMRI scanning. Note that in panels B and C the results were shown using box plot for all EEG electrode channels.

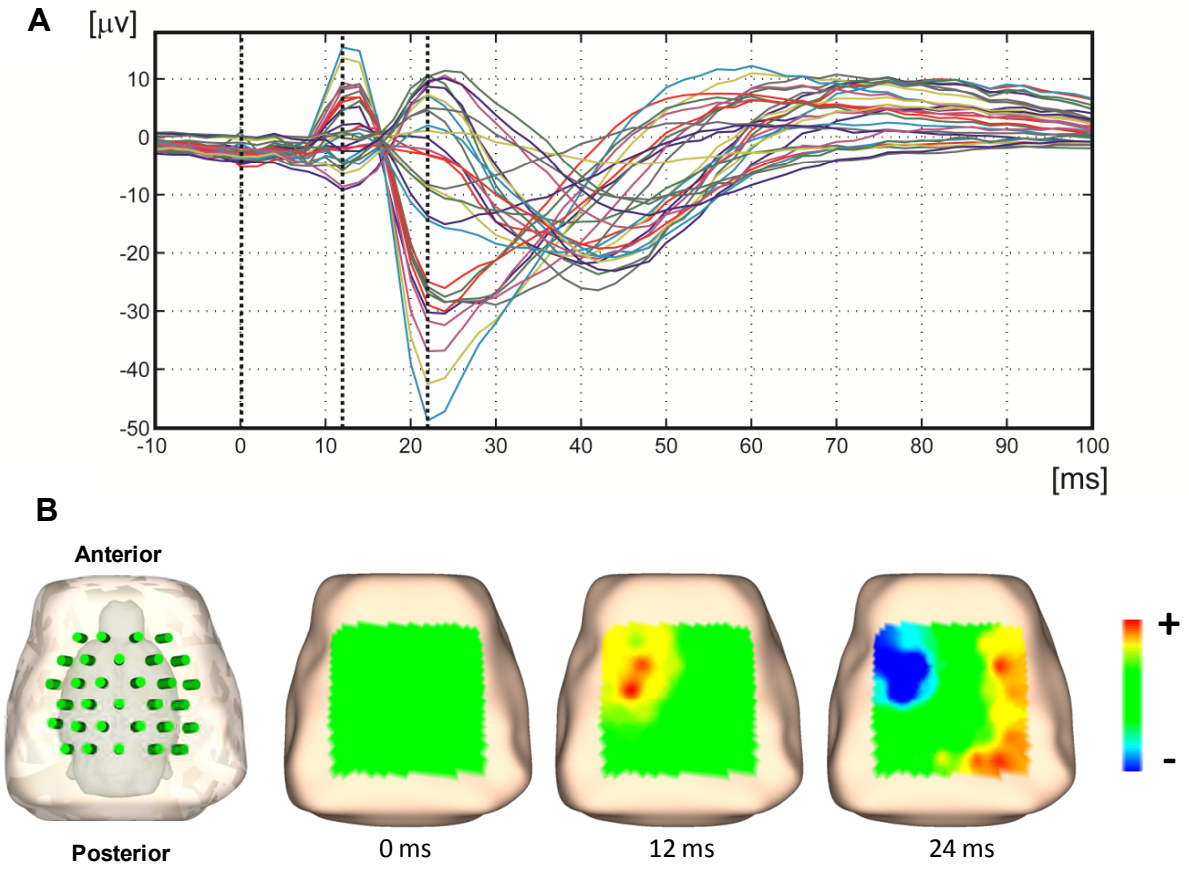


**Figure 4.10.** Somatosensory event-related potentials. (A) The grand average of the somatosensory event-related potentials for a single rat (all electrodes) obtained simultaneously with fMRI signals. Note that the timings for three components were marked on the average with vertical lines (0 ms, 12 ms and 24 ms). (B) The topographic maps of the somatosensory event-related potentials. These topographic maps were overlaid on the scalp surface of the particular Wistar rat, which was reconstructed from T1-weighted anatomical reference.

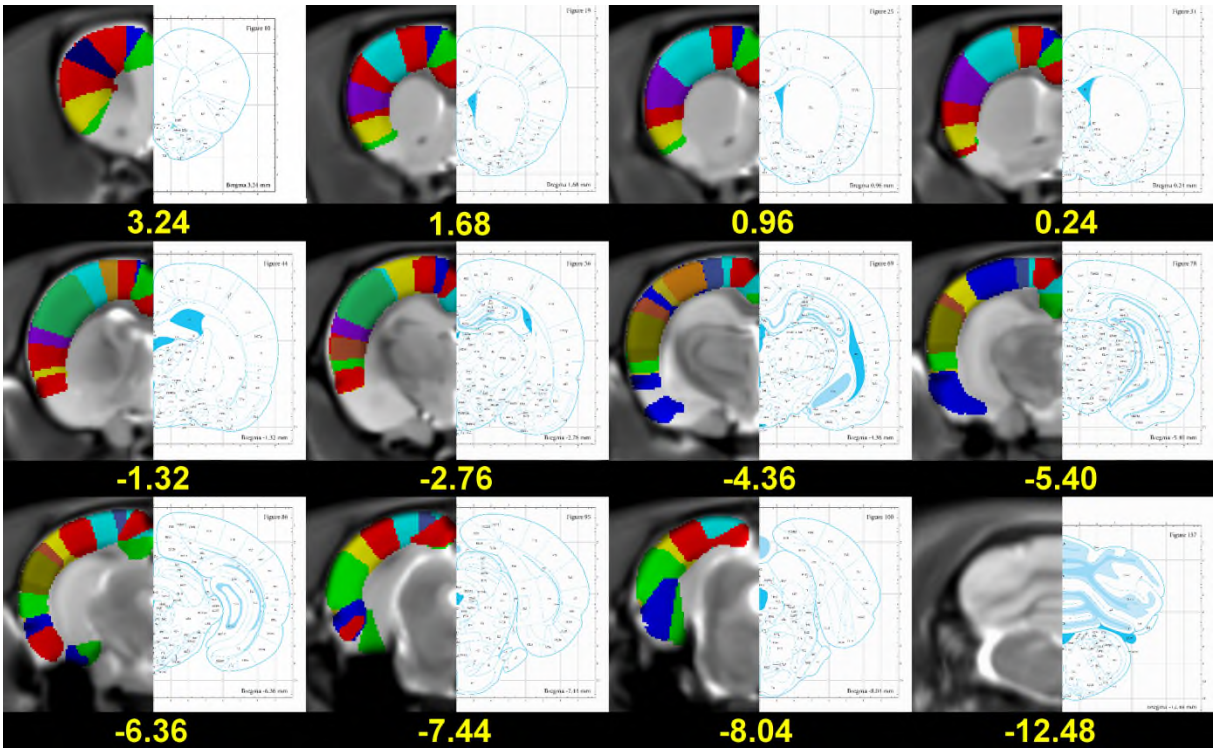


**Figure 4.11.** Left hemisphere of the coronal slices of the average template MRI with the digitalized atlas overlaid. The right hemisphere is the corresponding coronal slice of the atlas in the PDF book.

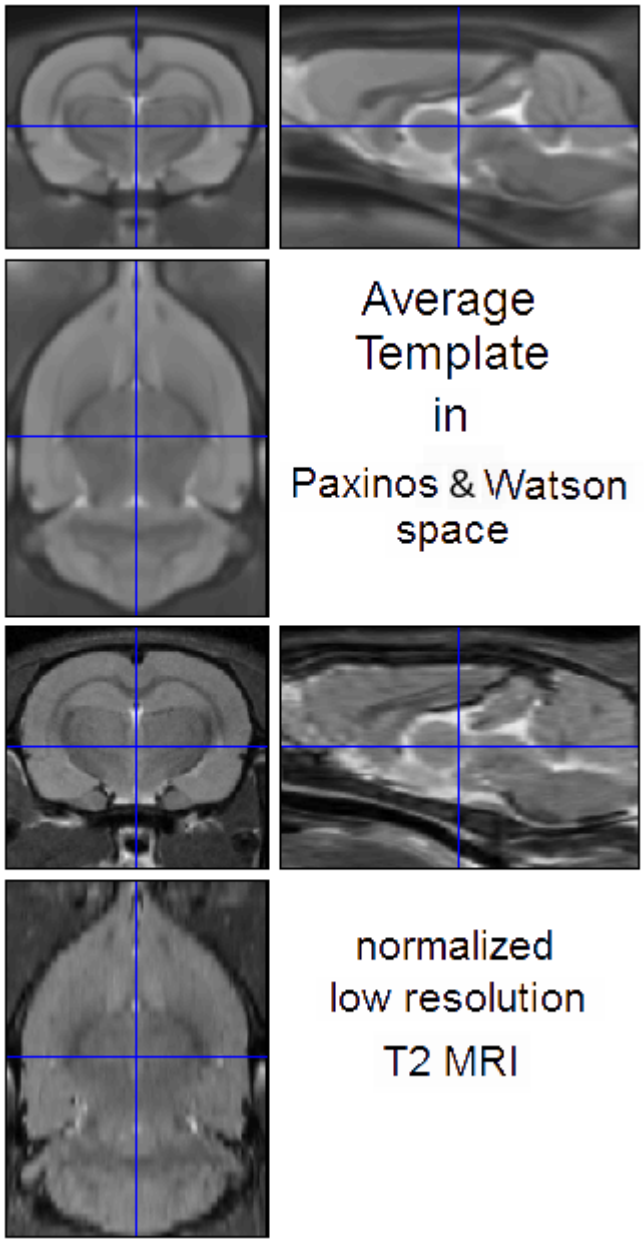


**Figure 4.12.** Registered orthogonal views of the spatially normalized low resolution MRI (bottom) and average MRI template (upper) constructed by the "Check Reg" button of SPM, which is the usual tool of SPM users for the visualization of registration results.

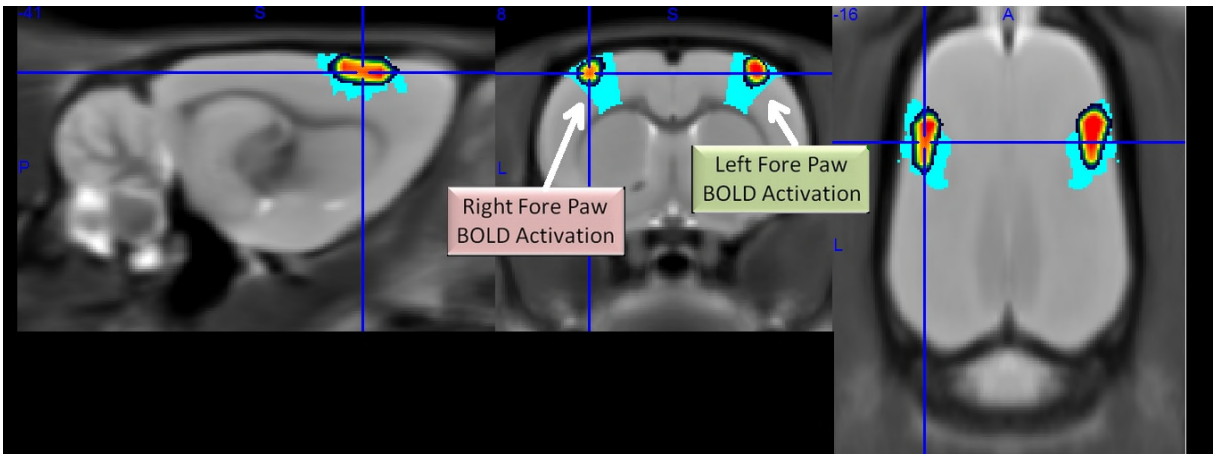


**Figure 4.13.** The fMRI activations of the both the left and right forepaw electrical stimulations. These are located within the contra-lateral forelimb regions of the somatosensory cortex.

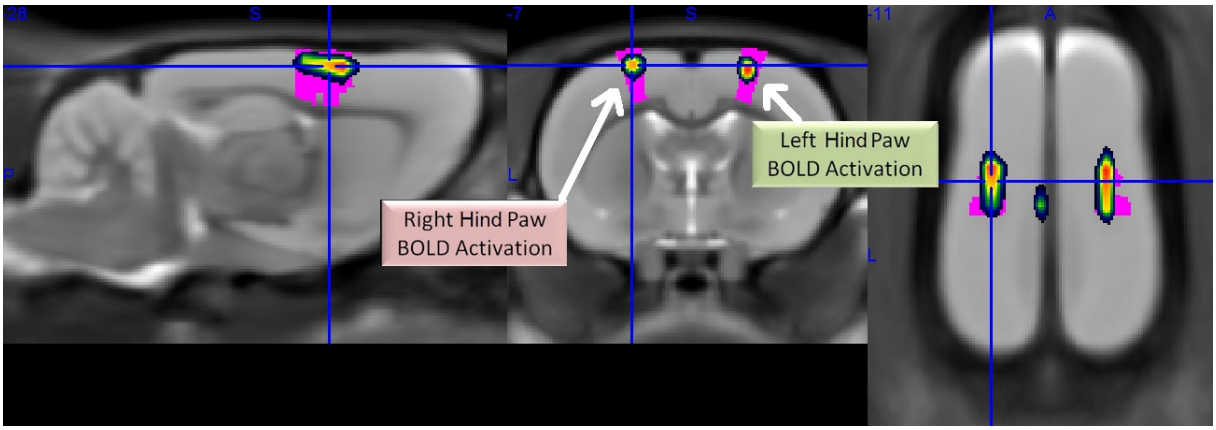


**Figure 4.14.** The fMRI activations of the both the left and right hindpaw electrical stimulations. These are located within the contra-lateral hindlimb regions of the somatosensory cortex.

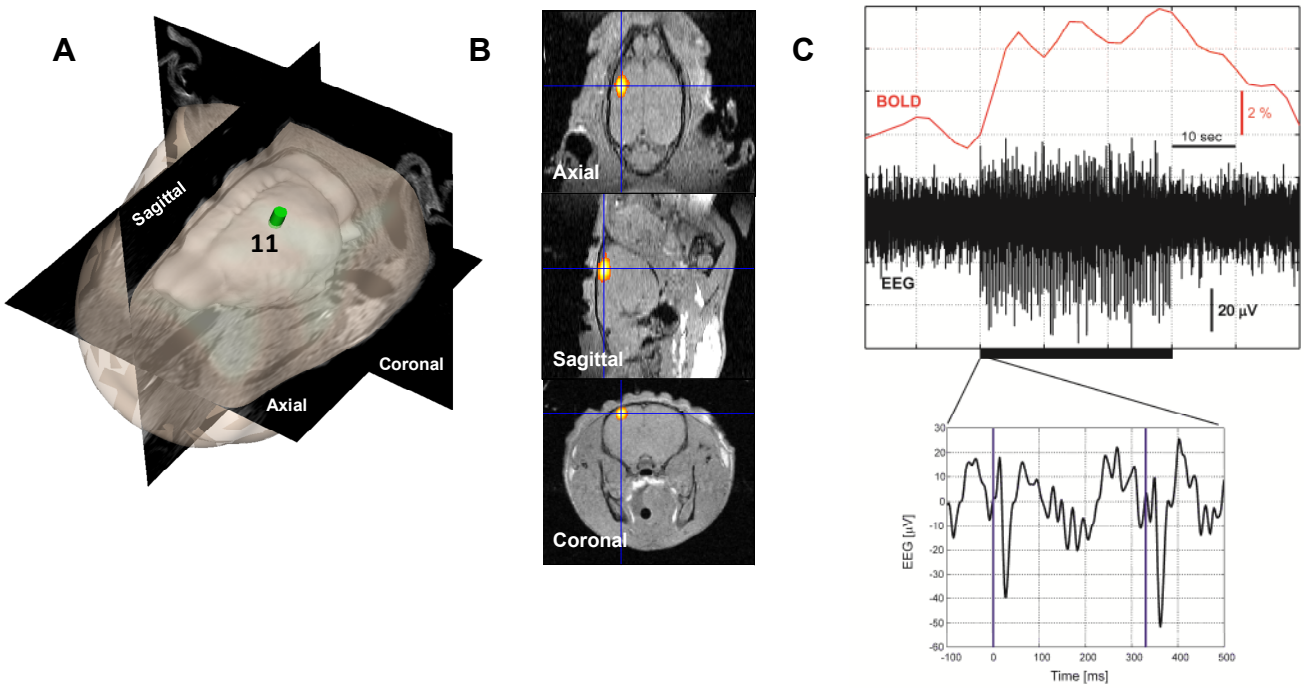


**Figure 5.1.** Simultaneous EEG and fMRI recording in a single rat. (A) The scalp and brain surfaces of the rat were constructed from T1-weighted anatomical reference. The green cylindrical object shows the position of the closest electrode to the fMRI activation area. (B) The SPM T-test score ($p < 0.05$) is co-registered on the individual T1-weighted anatomical reference. (C) The comparison of EEG (same channel above) and fMRI (ROI signal) data on the same time scale (upper panel). The black horizontal bar shows the stimulation period. The enlarged view of the EEG data from −100 to 500 ms (bottom panel). The blue line shows each stimulus onset.

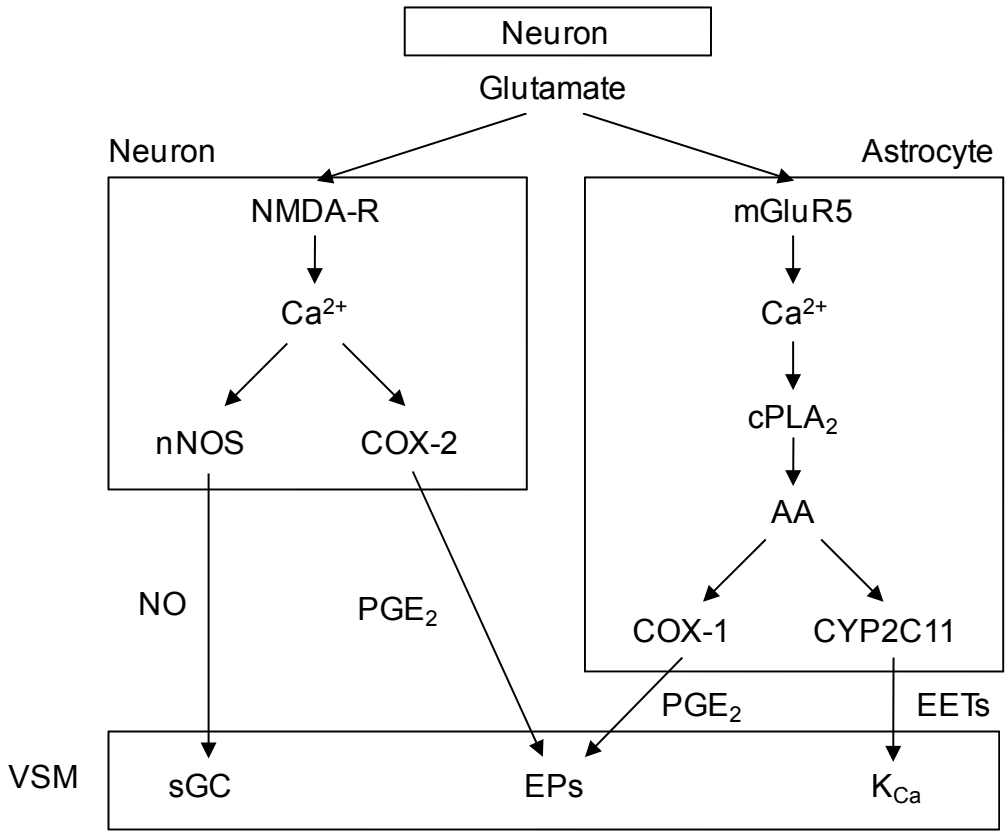


**Figure 5.2.** Schematic diagram of potential mechanisms of phasic/tonic modulatory pathways in neuron-to-vascular coupling. NO is generated by the $Ca^{2+}$-dependent coupling of neuronal NOS with *N*-methyl-D-aspartate (NMDA) receptor activation in neurons. NO can modulate cerebral vasodilation through stimulating soluble guanylyl cyclase (GC) in vascular smooth muscle (VSM). PGE2 is also generated $Ca^{2+}$-dependent coupling of COX-1 in neurons. Perisynaptic release of glutamate during neuronal activation is also thought to stimulate metabotropic glutamate receptors (mGluR5) on astrocytes and generate an increase in $Ca^{2+}$ that stimulates phospholipase $A_2$ ($PLA_2$). The consequent mobilization of AA could then provide substrate *1*) for astrocyte COX-1 to produce vasodilatory PGE2; *2*) for astrocyte CYP 2C11 to generate epoxyeicosatrienoic acids (EETs), which can produce vasodilation by opening VSM $K_{Ca}$ channels. Arrows with solid lines denote stimulatory effects.

# SECTION 11 LIST OF TABLES

| Combination | References |
|---|---|
| EEG–MRI | Ives et al., (1993)[48] |
| EEG–PET | Buchsbaum et al., (1984)[147] |
| EEG–NIRS | Hoshi et al., (1994)[148] |
| EEG–MEG | Salustri et al., (1989)[149] |
| MEG–NIRS | Mackert et al., (2004)[150] |
| MEG–MRI | Zotev et al., (2008)[151] |
| NIRS–PET | Villringer et al., (1997)[152] |
| NIRS–MRI | Kleinschmidt et al., (1996)[153] |
| PET–MRI | Judenhofer et al., (2008)[154] |

**Table 1.1.** Currently available simultaneous multimodal recording in humans and the related references in the literature.

| | T1 (ms) | T2 (ms) | T2* (ms) |
|---|---|---|---|
| Gray matter | 1322 ± 34 | 110 ± 4 | 51.8 ± 3.3 |
| White matter | 838 ± 18 | 74 ± 1 | 44.7 ± 1.2 |

**Table 1.2.** Typical NMR parameters of the human brain at 3 T reported in the literature[155] (Frontal gray/white matter).

| | 7.0 T | | 11.7 T | |
|---|---|---|---|---|
| | T2 (ms) | T2* (ms) | T2 (ms) | T2* (ms) |
| Gray matter | 50 ± 6 | 26 ± 9 | 38 ± 4 | 17 ± 4 |
| Corpus callosum | 40 ± 4 | 25 ± 3 | 33 ± 1 | 14 ± 2 |
| Primary somatosensory area (S1) | 49 ± 3 | 23 ± 3 | 36 ± 2 | 19 ± 3 |

**Table 1.3.** T2 and T2* in the rat brain reported in the literature[114].

| Reference | Animal | Electerode channel/material/position | MR scanner strength/bore/sequence | Anesthesia | Muscle relaxant |
|---|---|---|---|---|---|
| Brinker et al., (1999)[66] | Wistar rat | **2ch**/calomel/skull | 4.7T/12cm/T2*-weighted | α-chloralose (40mg/kg/90min, i.v.) | Pancuronium (0.2mg/kg/h) |
| Logothesis et al., (2001)[44] | Macaque monkey | **1ch**/platinum-iridium/ intracortical | 4.7T/40cm/GE-EPI | Fentanyl (3mg/kg, i.v.) and Isoflurane (0.3%) | Mivacurium (5mg/kg/h) |
| Opdam et al., (2002)[156] | Merino sheep | **10ch**/carbon/intracranial | 1.5T/human/EPI | Morphine (0.5mg/kg, i.v.) and Acepromazine (1.0mg) | Pancuronium (4mg) |
| Van Camp et al., (2003)[157] | Wistar rat | **2ch**/carbon/scalp | 7T/15cm/T2*-weighted | Halothane (2%) | Mivacurium (3mg/kg/h) |
| Nersesyan et al., (2004)[158] | WAG/Rij rat | **2ch**/carbon/subdermal | 7T/12cm/GE-EPI | Fentanyl (40mg/kg/45min, i.v.) and Haloperidol (1mg/kg/45min, i.p.) | D-tubocurarine (0.5mg/kg/h) |
| Mäkiranta et al., (2005)[159] | Piglet | **2ch**/carbon/subdermal | 1.5T/human/GE-EPI | Isoflurane (1.4–1.8%ET) | Pancuronium |
| Schmid et al., (2006)[160] | Macaque monkey | **10ch**/sintered Ag-AgCl/scalp | 4.7T/40cm/GE-EPI | Not used (conscious) | Not used |
| David et al., (2008)[161] | Epilepsy rat (GAERS) | **3ch**/carbon/skull | 2.35T/40cm/GE-EPI | Fentanyl (3μg/kg/h, i.v.) and Haloperidol (150μg/kg/h, i.p.) | D-tubocurarine (1.2mg/kg) |
| DeSalvo et al., (2010)[162] | Wistar rat | **2ch**/carbon/subdermal | 9.4T/16cm/GE-EPI | Fentanyl (40μg/kg, i.v.) and Haloperidol (1mg/kg, i.p.) | D-tubocurarine (0.5mg/kg) |

**Table 1.4.** Simultaneous recording of electrophysiology with functional MRI, a survey of the literature. The gray color shows those studies performed in rodents.

| Setting flow (ml/min) | Pressure (cm $H_2O$) | Expected tidal volume (ml) | Actual tidal volume (ml) |
|---|---|---|---|
| 800 | 20 | 8.0 | 3.6 |
| 700 | 18 | 7.0 | 3.3 |
| 600 | 16 | 6.0 | 2.6 |
| 500 | 12 | 5.0 | 2.0 |
| 400 | 10 | 4.0 | 1.4 |
| 300 | 8 | 3.0 | 1.0 |
| 200 | 5 | 2.0 | 0.6 |

**Table 3.1.** The parameter table of the ventilator settings (SAR-830/AP, CWE Inc., Ardmore, PA, USA). The data was obtained by using a water phantom under the similar setting in the rat experiment (respiration rate = 50, inspiration time = 0.6 s).

| Chemical composition | Property | Content (w%) |
|---|---|---|
| Polyoxyethylene cetyl ether | Emulsifier (surfactant) | 21.5 |
| Polyoxyethylene propylene glycol | Wetter (surfactant) | 3.5 |
| Glyceryl monostearate | Emulsifier (surfactant) | 3.5 |
| Sorbitan Trioleate (SPAN 85) | Emulsifier (surfactant) | 3.5 |
| Liquid paraffin | Stabilizer | 10.6 |
| Glycerine | − | 6.5 |
| Sodium chloride (NaCl) | − | 2.4 |
| 2,6-Di-tert-butyl-4-methylphenol (BHT) | Antioxidant | 0.2 |
| Sodium salicylate | Antiseptic | 0.3 |
| 2-(4-Thiazolyl) benzimidazole | Antiseptic | 0.6 |
| Coloring agent (orange) | − | 0.001 |
| Purified water | − | Rest |

**Table 3.2.** The chemical contents of EEG paste (Biotach, YGB103, GE Healthcare Japan, Tokyo, Japan) that has been utilized in EEG–fMRI experiments.

| Point | Description | P&W coordinates (mm) | Weight |
|---|---|---|---|
| Left Cortex | Leftmost point of the brain | (−7.92, −5.88, −5.28) | 2 |
| Right Cortex | Rightmost point of the brain | (7.92, −5.88, −5.28) | 2 |
| Bregma | Bregma | (0, 0, 0) | 2 |
| Interaural Center | Intersection between the medial plane and the Interaural line | (0, −9, 0) | 2 |

**Table 3.3.** Set of landmarks used for the affine registration.

| Landmark | Anatomical description | P&W coordinates (mm) | Weight |
|---|---|---|---|
| D M | The intersection between the caudal face of the cerebellum, the dorsal face of the medulla and the medial plane | (−0, −15, −7.44) | 2 |
| DC 7Cb | The middle of the slope of the dorsocaudal face of the 7th cerebellar lobe (*7Cb*) at the medial plane | (0,13.68, −3) | 3 |
| DR D3V | The most rostral point of the dorsal face of the dorsal 3rd ventricle (*D3V*) in the medial plane | (0, −1.56, −4.44) | 3 |
| C bas | The middle of the basilar artery (*bas*) in the medial plane | (0, −11.40, −11.16) | 2 |
| C PFl (R,L) | Center of the paraflocculus (*PFl*) | (±6.96, −11.40, −7.44) | 2 |
| R 2Cb | The most rostral point of the second cerebellar lobe (*2Cb*) in the medial plane | (0, −8.40, −5.16) | 1 |
| D fmj (R,L) | Posterior and dorsal point of the major forceps (*fmj*) | (±2.76, −7.92, −2.40) | 3 |
| V fmj (R,L) | The same as above but ventral | (±4.80, −7.92, −4.20) | 3 |
| alv-cc (R,L) | A point in the boundary between the alveus of the hippocampus (*alv*) and the corpus callosum | (±5.40, −6.60, −6.96) | 3 |
| D MZMG (R,L) | The most posterior and dorsal contact between the marginal zone of the medial geniculate nucleus (*MZMG*) | (±3.48, −6.36, −5.04) | 2 |
| V MZMG (R,L) | The same as above but the most ventral point | (±3.96, −6.36, −6.48) | 2 |
| C scc | The most caudal point of the splenium of the corpus callosum (*scc*) in the medial plane. | (0, −5.16, −3.24) | 1 |
| R IPF | The most rostral point of the interpeduncular fossa (*IPF*) in the medial plane. | (0, −5.04, −8.52) | 2 |
| D cc (R,L) | The most dorsal point of the corpus callosum | (±2.52, −4.80, −2.04) | 2 |
| pc | The most posterior point of the posterior commisure (*pc*) in the medial plane | (0, −4.68, −5.04) | 1 |
| V PLCo1 (R,L) | The most ventral point of the posterior-lateral cortical amygdaloid nucleus, layer 1 (*PLCo1*) | (±4.68, −3.24, −10.32) | 2 |

| | | | |
|---|---|---|---|
| ic-ec (R,L) | Intersection between the internal capsule (*ac*) and the external capsule (*ec*) | (±5.28, −3.24, −4.68) | 2 |
| LV (R,L) | Center of the most lateral and dorsal region of the lateral ventricle (*VL*) or choroid plexus (*chp*) | (±1.80, −0.72, −3.36) | 3 |
| 3V-cc (R,L) | Corpus callosum at the level of the center of the 3rd ventricle (*3V*) | (±5.04, −0.48, −6.36) | 3 |
| ac | The most anterior point of the anterior commisure (*ac*) in the medial plane | (0, −0.12, −6.84) | 1 |
| V rcc | The most ventral point of the rostrum of the corpus callosum (*rcc*) | (0,1.80, −5.04) | 1 |
| R fmi (R,L) | Rostral point of the major forceps (*fmi*) | (±2.04,4.20, −3.24) | 3 |
| R FrA (R,L) | Rostral frontal area (*FrA*), above the glomelurar layer of the olfactory bulb (*Gl*) | (±1.20,6.48, −2.16) | 2 |

**Table 3.4.** Set of landmarks used for the ATPS registration.

| Rat | With EEG mini-cap (dB) | Without EEG mini-cap (dB) |
|---|---|---|
| Rat #1 | 27.2 | 27.1 |
| Rat #2 | 25.3 | 28.4 |
| Rat #3 | 25.4 | 28.5 |
| Rat #4 | 27.5 | 28.3 |
| Rat #5 | 26.8 | 28.2 |
| Rat #6 | 25.2 | 28.5 |
| Rat #7 | 25.4 | 28.8 |
| Rat #8 | 24.7 | 28.6 |
| Rat #9 | 25.5 | 28.7 |
| Rat #10 | 27.1 | 28.3 |
| Rat #11 | 26.2 | 27.6 |
| Rat #12 | 25.5 | 28.5 |
| Average | 26.0 | 28.3 |
| Std | 0.9 | 0.5 |

**Table 4.1.** The transmitter pulse attenuation adjusted by using the protocol provided by Bruker Biospin (AdjRefG, Paravision 5.0) ($n$ = 12).

| Domain | Parameter | | With EEG mini-cap | Disconnected EEG mini-cap | Without EEG mini-cap |
|---|---|---|---|---|---|
| Time | SPM t-score (p<0.001) | | 12.4 ± 2.4 | 12.8 ± 2.0 | 13.5 ± 4.8 |
| | Standard deviation (%) | | 2.98 ± 0.55 | 2.62 ± 0.35 | 2.57 ± 0.54 |
| Space | Paxinos atlas (mm) | X | −3.76 ± 0.46 | −3.56 ± 0.17 | −3.68 ± 0.34 |
| | | Y | 0.36 ± 0.36 | 0.32 ± 0.33 | 0.08 ± 0.46 |
| | | Z | −2.24 ± 0.43 | −2.32 ± -0.23 | −2.32 ± 0.48 |
| | Activate area “size” (p<0.001) | | 1301 ± 759 | 1497 ± 323 | 1657 ± 1221 |

**Table 4.2.** The summary of the fMRI experiment ($n$ = 5). Several parameters were compared in three different conditions.

| Physiological parameter | Units | Mean | s.d. |
|---|---|---|---|
| Body weight | g | 200 | 8 |
| Heart rate | beats/min | 497 | 22 |
| Blood pressure | mmHg | 96 | 19 |
| Rectal temperature | degree | 35.8 | 0.3 |
| $pO_2$ | mmHg | 113.1 | 11.9 |
| $pCO_2$ | mmHg | 44.0 | 3.1 |
| pH | – | 7.303 | 0.042 |
| Oxygen saturation | % | 91.3 | 2.4 |
| End-tidal $CO_2$ | mmHg | 22.2 | 4.0 |
| Hematocrit | % | 38.6 | 3.6 |
| Hemoglobin | g/dL | 12.6 | 1.2 |
| Glucose | mg/dL | 158.4 | 36.5 |
| Lactate | mmol/L | 1.6 | 0.7 |

**Table 5.1.** The physiological variables of Wistar rats obtained during simultaneous EEG and fMRI experiments ($n$ = 5).

| Disease | Reference | Model | MRI technique |
|---|---|---|---|
| Epilepsy | Tenny et al., (2003)[163] | Absence seizures | EEG–fMRI |
| | Nersesyan et al., (2004)[158] | Absence and generalized tonic-clonic | EEG–fMRI |
| | Englot et al., (2008)[164] | Secondarily generalized limbic seizures | EEG–fMRI |
| | David et al., (2008)[161] | GAERS | EEG–fMRI |
| Alzheimer | Wadghiri et al., (2003)[165] | APP and APP/PS1 | Contrast agent |
| | Wu et al., (2004)[166] | APP (V717F, K670N/M671L) | CBV |
| | Higuchi et al., (2006)[167] | APP | $^{19}$F labeling |
| | Lau et al., (2008)[168] | APP/PS1 | Morphometry |
| Parkinson | Pelled et al., (2005)[169] | 6-OHDA | Resting fMRI |
| | Van Camp et al., (2009)[170] | 6-OHDA | DTI |
| | Hou et al., (2010)[171] | 6-OHDA | MRS |
| Stroke | Beckman et al., (1999)[172] | MCAO | Angiography |
| | Li et al., (2000)[173] | MCA suture | DTI |
| | Aoki et al., (2003)[174] | MCAO | MEMRI |
| Spinal cord injury | Ramu et al., (2006)[175] | Moderately severe injury | fMRI |
| | Endo et al., (2007)[99] | Completely cut injury | fMRI |
| | Takagi et al., (2009)[176] | Contusive injury | DTI |
| | Ghosh et al., (2010)[177] | Spinal cord injury | fMRI |
| Depression | Huang et al., (2011)[178] | Flinders sensitive line | fMRI |
| Pain | Heindl-Erdmann et al., (2010)[179] | DREAM knockout | fMRI |

**Table 5.2.** The study of animal disease models, demonstrating its feasibility of various MRI sequences in animal MR scanner.